











## REPORT DOCUMENTATION PAGE

Form Approved  
OMB No 0704-0188

1a REPORT SECURITY CLASSIFICATION <b>UNCLASSIFIED</b>				1b RESTRICTIVE MARKINGS			
2a SECURITY CLASSIFICATION AUTHORITY				3 DISTRIBUTION/AVAILABILITY OF REPORT <b>Approved for public release distribution unlimited.</b>			
2b DECLASSIFICATION/DOWNGRADING SCHEDULE							
4 PERFORMING ORGANIZATION REPORT NUMBER(S)				5 MONITORING ORGANIZATION REPORT NUMBER(S)			
6a NAME OF PERFORMING ORGANIZATION Naval Postgraduate School		6b OFFICE SYMBOL (If applicable) 33		7a NAME OF MONITORING ORGANIZATION Naval Postgraduate School			
6c ADDRESS (City, State, and ZIP Code) Monterey, CA 93943-5000				7b ADDRESS (City, State, and ZIP Code) Monterey, CA 93943-5000			
8a NAME OF FUNDING SPONSORING ORGANIZATION		8b OFFICE SYMBOL (If applicable)		9 PROCUREMENT INSTRUMENT IDENTIFICATION NUMBER			
8c ADDRESS (City, State, and ZIP Code)				10 SOURCE OF FUNDING NUMBERS			
				PROGRAM ELEMENT NO	PROJECT NO	TASK NO	WORK UNIT ACCESSION NO
11 TITLE (Include Security Classification) THEORY FOR THE CEBAF INFRARED AND SHIPBOARD FELS							
12 PERSONAL AUTHOR(S) Clark, Darwin L.							
13a TYPE OF REPORT Master's Thesis		13b TIME COVERED FROM TO		14 DATE OF REPORT (Year, Month, Day) March 1992		15 PAGE COUNT 81	
16 SUPPLEMENTARY NOTATION The views expressed in this thesis are those of the author and do not reflect the official policy or position of the Department of Defense or the U.S. Govt							
17 COSATI CODES			18 SUBJECT TERMS (Continue on reverse if necessary and identify by block number)				
FIELD	GROUP	SUB-GROUP	Shipboard laser Optical Mode distortion				
			FEL theory Multiple Pass distortion				
			CEBAF FEL Design				
19 ABSTRACT (Continue on reverse if necessary and identify by block number) The continuing development of the free electron laser (FEL) as a powerful and versatile source of coherent radiation steadily drives toward the goal of high efficiency and broad tunability at shorter wavelengths. New experiments provide significant data and insight for analysis by theoreticians and experimentalists. Two important areas of study are short electron pulse effects, and the dynamics of optical mode distortion by intense beam currents. The initial part of this thesis examines one aspect of the projected task of FEL application as a military weapon. The advantages of the FEL over other directed energy sources are detailed, as well as the challenge presented by the effects of the marine atmosphere to high energy laser propagation. The remainder of this thesis examines several effects of long wavelength FELs. Chapter IV examines the proposed parameters of the CEBAF IR FEL, and the analysis leads to predictions describing system performance. Chapter V examines the effects of single							
20 DISTRIBUTION/AVAILABILITY OF ABSTRACT <input checked="" type="checkbox"/> UNCLASSIFIED/UNLIMITED <input type="checkbox"/> SAME AS RPT <input type="checkbox"/> DTIC USERS				21 ABSTRACT SECURITY CLASSIFICATION Unclassified			
22a NAME OF RESPONSIBLE INDIVIDUAL Prof W.B. Colson				22b TELEPHONE (Include Area Code) (408) 646-2765		22c OFFICE SYMBOL PH/Cw	

pass optical mode distortion for FELs with narrow electron beams. Single-mode theory states that gain is proportional to the product of electron beam current and filling factor, but three-dimensional simulations show that gain is a function of electron beam filling factor alone. Also examined is a phenomenon of destructive interference of light in the FEL undulator.

Chapter VI extends the analysis of the relationship of gain and beam size to include multiple passes of laser light through the laser resonator. This affirms the general gain relationship, where gain is a function of electron beam filling factor, and also further explores the phenomenon of destructive interference within the optical mode.

Approved for public release; distribution is unlimited.

**THEORY FOR THE CEBAF INFRARED AND SHIPBOARD FELS**

by

**Darwin L. Clark**

Lieutenant, United States Navy

BS., United States Naval Academy 1986

Submitted in partial fulfillment of the  
requirements for the degree of

**MASTER OF SCIENCE IN PHYSICS**

from the

**NAVAL POSTGRADUATE SCHOOL**

March 1992



17003  
C4807-1  
C.1

## ABSTRACT

The continuing development of the free electron laser (FEL) as a powerful and versatile source of coherent radiation steadily drives toward the goal of high efficiency and broad tunability at shorter wavelengths. New experiments provide significant data and insight for analysis by theoreticians and experimentalists. Two important areas of study are short electron pulse effects, and the dynamics of optical mode distortion by intense electron beam currents.

The initial part of this thesis examines one aspect of the projected task of FEL application as a military weapon. The advantages of the FEL over other directed energy sources are detailed, as well as the challenge presented by the effects of the marine atmosphere to high energy laser propagation.

The remainder of this thesis examines several effects of long wavelength FELs. Chapter IV examines the proposed parameters of the CEBAF IR FEL, and the analysis leads to predictions describing system performance. Chapter V examines the effects of single pass optical mode distortion for FELs with narrow electron beams. Single-mode theory states that gain is proportional to the product of electron beam current and filling factor, but three dimensional simulations show that gain is a function of electron beam filling factor alone. Also examined is a phenomenon of destructive interference of light in the FEL undulator.

Chapter VI extends the analysis of the relationship of gain and beam size to include multiple passes of laser light through the laser resonator. This affirms the general gain relationship, where gain is a function of electron beam filling factor, and also further explores the phenomenon of destructive interference within the optical mode.



## Table of Contents

I. INTRODUCTION .....	1
II. THE SHIPBOARD FREE ELECTRON LASER .....	3
A. INTRODUCTION .....	3
B. THREAT ENVIRONMENT .....	3
C. HEL OPTIONS .....	4
D. ATMOSPHERIC PROPAGATION EFFECTS .....	7
III. FREE ELECTRON LASER THEORY .....	16
A. BASIC FREE ELECTRON LASER PHYSICS .....	16
B. ELECTRON DYNAMICS .....	21
C. ENERGY EVOLUTION .....	22
D. THE PENDULUM EQUATION .....	24
E. THE WAVE EQUATION .....	26
F. DIMENSIONLESS PARAMETERS .....	28
IV. THE CEBAF INFRARED FEL DESIGN .....	30
A. BACKGROUND .....	30
B. CEBAF IR FEL PARAMETERS .....	32
C. SHORT-PULSE EFFECTS .....	34
D. CEBAF IR FEL TUNING RANGE AND GAIN .....	44
V. OPTICAL MODE DISTORTION .....	47
A. BACKGROUND .....	47
B. GENERAL MODE DISTORTION .....	47

C. MODE DISTORTION SIMULATIONS .....	48
D. MODE PARAMETERS, RESONANCE AND GAIN .....	54
E. GAIN AND SMALL ELECTRON BEAMS .....	57
F. PROPAGATION AND INTERFERENCE .....	59
VI. MULTI-PASS OPTICAL MODE DISTORTION .....	62
A. BACKGROUND .....	62
B. MULTIPLE PASS PROPAGATION AND INTERFERENCE .....	62
C. GAIN AND SMALL ELECTRON BEAMS OVER MULTIPLE PASSES .....	66
VII. CONCLUSIONS .....	69
LIST OF REFERENCES .....	70
INITIAL DISTRIBUTION LIST .....	72

## ACKNOWLEDGEMENT

The author gratefully acknowledges the guidance and support of Dr. W. B. Colson.





# **I. INTRODUCTION**

A free electron laser (FEL) produces light through the stimulated emission from a high energy electron beam in a periodic magnetic field. Proposed by J. M. J. Madey in 1970 [1], the FEL has great potential for development as a highly efficient, powerful coherent light source with medical, industrial, and military applications.

Theoretical models and technological demonstrations are extending the limits of FEL performance, with high power and efficiency possible within a few years. The FEL is a significant tool because of its unique operating characteristics. Among these are the use of electricity as the power source, order of magnitude tunability of output wavelength, and high "wallplug" efficiency. With the likely development of FEL power into the tens of megawatt range, the potential exists for military applications. Ground based and space based options have been studied by the Strategic Defense Initiative Office (SDIO). The option of arming a naval vessel with a high energy laser as an air defense weapon deserves study, and is discussed here in Chapter II.

Chapter III provides a foundation of FEL theory to enable detailed descriptions of FEL performance in subsequent chapters. Chapter IV examines the infrared (IR) FEL proposed for the Continuous Electron Beam Accelerator Facility (CEBAF), of Newport News, Va. The planned accelerator and FEL parameters are analyzed to assist design performance optimization. The tuning range of the CEBAF IR FEL is analyzed to determine the influence of short electron pulse effects on FEL gain and power.

Chapter V treats optical diffraction, and the phenomenon of optical mode distortion caused by intense electron beams. Single-mode gain theory, which neglects the effects of diffraction and mode distortion, is shown to be inadequate. Using three-dimensional simulations of the optical mode wave front, a relationship between single-pass gain and electron beam size, accounting for diffraction and distortion, is found. A curve is generated which is generally applicable to all FELs with small electron beams. Chapter VI explores the new gain relationship and predicted destructive interference phenomena in a multiple-pass simulation. A similar gain curve is generated.



## **II. SHIPBOARD FREE ELECTRON LASER**

### **1. INTRODUCTION**

The current state-of-the-art anti-ship missile (ASM) threat posed to the U.S. Navy consists of high speed, maneuverable, robust and electronically sophisticated weapons. Current Fleet defensive weapons and tactics center on the highly complex Aegis Combat Systems Suite, which integrates sensors, fire control, and decision aids with surface-to-air missiles (SAMs). The Achilles' Heel of this system is the limited number of SAMs and their performance limitations. High Energy Laser (HEL) design concepts have been studied for incorporation into combat ships for air defense. The Free Electron Laser (FEL), due to its design and performance characteristics, would be the optimal choice for a future ship based HEL weapon.

### **2. THREAT ENVIRONMENT**

Combating the high speed and possible high density of anti-ship guided missiles is among the highest priority missions of tactical naval planning for the next generation of shipboard weapon systems. ASMs, capable of launch from submerged submarines, tactical aircraft, and small patrol boats are cheap, reliable and difficult to defeat with all but the most complex integrated systems. In worst-case wargaming scenarios, which include numerous ASMs simultaneously converging from many directions, even the most advanced air defense system, such as an Aegis-equipped guided missile cruiser, can be overwhelmed through exhaustion of the SAMs carried. This is known as the

"magazine depth."

Time is also considered a highly limiting factor for anti-ship missile defense. With present systems, once a target is identified, evaluated as a threat and the order is given to engage, there is a time lag due to SAM flight to intercept the target lasting from ten seconds for a close range engagement to two minutes for a longer range target. If the target is not destroyed, this process must be repeated, further wasting time and valuable defensive missiles. The Aegis system can successfully track and engage several incoming missiles simultaneously, but is ultimately limited by its magazine depth.

### **3. HEL OPTIONS**

HELs, having been the subject of extensive research since the initiation of the Strategic Defense Initiative (SDI) program in 1983, are usually categorized by the fuel sources that drive them. These include X-Ray Lasers, Excimer or Chemical Lasers, and Free Electron Lasers.

X-Ray Lasers, despite characteristics desirable for exoatmospheric SDI missions, are not a feasible option for a shipboard HEL. The wavelength of radiation produced by these lasers, in the X-Ray region, does not propagate effectively in the atmosphere, rendering it somewhat useless as a shipboard weapon. More importantly, the laser is powered by the detonation of a nuclear weapon, which understandably obviates further discussion of its adoption by the fleet.

Chemical lasers, having been tested successfully as HELs, are a much more attractive option for a shipboard weapon. The MIRACL laser system, employing a deuterium fluoride (DF) laser, successfully destroyed a target

drone aircraft at White Sands Missile Range. This laser emits light in a favorable wavelength for atmospheric use (  $3.7\text{--}4.0\mu$  ) [2], and has been studied for possible shipboard use. The main obstacle for use of chemical lasers is the storage and combustive reaction of the highly volatile agents needed to drive the laser. The exhaust gases of chemical lasers are highly toxic and would require a complex air filtration and cleanup system to enable habitability for the crew of a vessel equipped with a chemical laser.

Chemical lasers are driven through the exothermic reactions of highly volatile oxidizer and fuel streams which are mixed inside the optical cavity. The reactive nature which enables these agents to be useful is itself a strong reason for the rejection of chemical lasers as shipboard weapons. The transport and storage of highly pressurized, toxic, and reactive chemicals to ships at sea would require designs of replenishment ships (tankers and supply ships) that today do not exist. The potential for disaster once the chemicals were aboard the laser ship would necessitate detailed and expensive safety programs, further complicating the process. Ultimately, the chemically driven laser system would fall victim to the same limitations of the missile systems it would seek to replace. The chemical laser is driven by an irreversible chemical reaction that would cease once the fuel and oxidizer were exhausted. This is a solid magazine depth that would severely limit the duration of engagement and require complex reloading procedures. This is a major flaw for a plan to field a chemical HEL aboard a ship. A principle advantage of a ship as a weapons platform includes long endurance on station, and it would be wasteful of this endurance potential to place a short-legged weapon aboard as a principle means of air defense for a battle group or geographic region.



A simpler and more logical system for deployment of HELs for near and long term use would involve development of an aircraft-based chemical HEL, followed later by the development of a shipboard FEL (SFEL) when the necessary technology matures. Aircraft lack the endurance of ships, needing to land frequently for fuel, maintenance and crew rest, so that the engage-and-reload requirements for a chemical HEL would not represent as severe a mission limiting factor as would be the case for a shipboard chemical HEL. The lessons learned through development of the aircraft based HEL would later benefit the deployment of the SFEL.

The Free Electron Laser has several advantages over other potential HEL designs. The principle advantage of this system is the wide range of wavelengths over which the FEL can be tuned. This allows the FEL to be tuned to exploit highly variable atmospheric conditions and to be more highly resistant to countermeasures. An additional advantage, crucial when considering distribution of large quantities of electricity aboard ships, is that scaling up to allow the addition of an FEL would be simply a matter of adding more generators and power conditioning equipment. Recent technological advances in capacitor storage banks would allow large quantities of electrical energy to be held in reserve for immediate use, providing a quick reaction capability for the SFEL. This is an easily manageable task, and would fall in well with the navy's future plans for an integrated electric drive combatant vessel. An especially attractive factor of FEL design is the generally accepted "wallplug" efficiency goal of 40%. This is would be made possible through use of an energy recovery system, which would also enable reduction of the necessary mass of radiation shielding. The limiting factor for the operation of the FEL would then be the common fuel supply used for propulsion and

electricity of the ship, which is already supported by a well established system.

#### 4. ATMOSPHERIC PROPAGATION EFFECTS

The marine atmospheric environment within which an SFEL would operate is a highly variable, dynamic system with numerous linear and nonlinear effects that have profound influence on the propagation of high-power laser beams. In addition to the effect of optical diffraction within the atmosphere, there exist atmospheric attenuation effects. The mechanisms of laser beam photon loss through atmospheric attenuation by the constituents suspended in the atmosphere can be broken down into several distinct effects: the linear absorption and scattering of the molecular and aerosol elements in the atmosphere, the random wander, spreading, and distortion of the laser beam due to the effects of turbulence within the atmosphere, and the non-linear defocusing effects of thermal blooming caused by the absorption of small amounts of beam power by the atmosphere. These effects are dependent on atmospheric temperature, clarity, humidity, wind velocity, and beam characteristics such as wavelength, temporal operating mode and beam diameter.

Accounting solely for linear atmospheric effects, the mean peak irradiance of a propagating laser beam is  $I_P = [P/(\pi w^2)] \exp(-\alpha_T z)$ , where  $P$  is the transmitted laser power,  $z$  is the range, and  $\alpha_T$  is the atmospheric extinction or attenuation coefficient. The term  $w$  is the root mean square (rms) beam radius and is a function of many factors,  $w = \sqrt{w_d^2 + w_j^2 + w_t^2}$ , where  $w_d$  is a factor of diffraction and beam quality,  $w_j$  accounts for beam jitter, and  $w_t$  is a correction for atmospheric turbulence [3].

The diffraction and beam quality factor correction is  $w_d = \sqrt{\beta^2 z^2 / k^2 w^2 + w^2 (1 - z/R)^2}$ . Here  $\beta$  is a ratio of actual focal spot radius to the diffraction limited spot radius, or

$$\beta = \frac{1/e \text{ Radius of actual focal spot}}{1/e \text{ Radius of Diff. Limited spot}} = \frac{w_d}{w_{ideal}}, \quad w_{ideal} = w(z)/\sqrt{2}. \quad 2-1$$

Range  $R$  can be varied from  $R = z$  for a beam focussed to the point at distance  $z$ , to  $R = \infty$  for a collimated beam. Beam jitter effects are corrected for by the addition of the mean square radial displacement of the focal spot,  $w_j = \sqrt{2\langle\theta_x^2\rangle z^2}$ , at range  $z$  for a varying single axis jitter angle,  $\langle\theta_x^2\rangle$ . This angle is isotropic for  $x$  and  $y$  axes, so that  $\langle\theta_x^2\rangle = \langle\theta_y^2\rangle$ .

The attenuation and extinction term,  $\alpha_T = \alpha_{abs} + \alpha_{scat}$ , represents the effects of absorption and scattering of molecular and aerosol components of the atmosphere. Scattering is a directional redistribution of the beam incident on the various molecules composing the atmosphere. This does not reduce the energy of the beam but does reduce the intensity. Absorption is a very complicated and irregular function of beam wavelength, and is a critical factor in the effects of thermal blooming. Scattering and absorption by aerosol components is generally less dependent on wavelength than molecular absorption and scattering. The slight wavelength dependence of the absorption and scattering coefficients is a result of the combined effects of the aerosol complex refractive index and the size distribution of the aerosol particles. Aerosol effects become somewhat significant at shorter wavelengths ( $\lambda \leq 3\mu m$ )[3]. Fig 2-1 shows the highly variable nature of the aerosol and molecular effects.



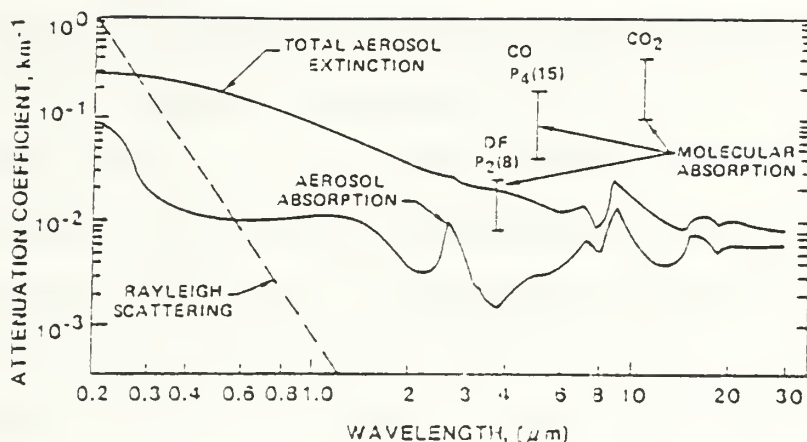


Figure 2-1: Calculated aerosol absorption and extinction by the atmosphere in 23km visibility vs. wavelength [3].

Figure 2-1 is generated through a model of the continental atmosphere. The marine environment would include higher levels of humidity and its effects. Included on the graph are range bars indicating the wavelengths of three common lasers and the variation of the attenuation coefficients for each. Of note is the dip in aerosol absorption effects for  $\lambda \approx 3.8\mu\text{m}$ , which closely corresponds to the wavelength of the DF laser. This wavelength is near an optimum wavelength selected for the study of FEL placement on a naval vessel [4].

Atmospheric transmittance, accounting for molecular and aerosol absorption and scattering effects, is a ratio of initial irradiance,  $I_0$ , to that at a range  $z$  :

$$T = \frac{I(z)}{I_0} = \exp\left\{-\int_0^z \alpha_T dz\right\}. \quad 2-2$$

Atmospheric turbulence arises from convective air currents and eddies caused by air-surface temperature gradients, which result in slight fluctuations in the index of refraction. For beam propagation, the eddies form pockets of disturbed air, known as "turbules", which vary in size relative to the beam diameter. This non-uniformity results in the various effects of beam wandering off the target, intensity fluctuations across the beam profile, and spreading of the beam spot size. Turbulent beam spread and wander effects are accounted for by the term  $w_t \approx 2z/kL_0$  where  $z$  is distance,  $k$  is the wave number, and  $L_0 = (0.545k^2C_N^2z)^{-3/5}$  is the lateral coherence length of a spherical wave.  $C_N^2$  is the refractive index structure constant. Figure 2-2 shows wavelength dependence of the effects of beam spreading and wander on average irradiance,  $I(\lambda)$ , normalized by the irradiance at  $\lambda = 10\mu\text{m}$  [3]. At long ranges, turbulent beam spreading becomes wavelength independent, but this is an exceptional regime. In the usual case, the turbulence coefficient  $w_t = 2.01(\lambda^{-1/5}C_N^{6/5}z^{8/5})$ . Though the dependence of turbulent beam spread on  $\lambda^{-1/5}$  is relatively weak, this relationship implies that there is an optimum wavelength for propagation for given values of turbulence level, range, and aperture diameter (diffraction being proportional to  $\lambda$ ). Neglecting jitter effects, the mean peak intensity is given by

$$I \propto \frac{1}{w_d^2} \frac{1}{1 + w_t^2/w_d^2}. \quad 2-3$$

Assuming a reference wavelength  $\Lambda_0$ , the ratio of the irradiances

$$\frac{I(\lambda)}{I(\Lambda_0)} = \left\{ \frac{\Lambda_0}{\lambda} \right\}^2 \frac{1 + A}{1 + A(\Lambda_0/\lambda)^{12/5}}. \quad 2-4$$

where  $A = 16.12\pi^2 w^2 (C_N^2 z \Lambda_0^{-2})^{-6/5} / \beta^2$ . For wavelengths shorter than the critical

wavelength, defined by  $\lambda_c = (A/5)^{5/12} \Lambda_0$ , the effects of turbulent spreading dominate the diffraction limited focusing, and beam intensity decreases as  $\lambda^{2/5}$  [3].

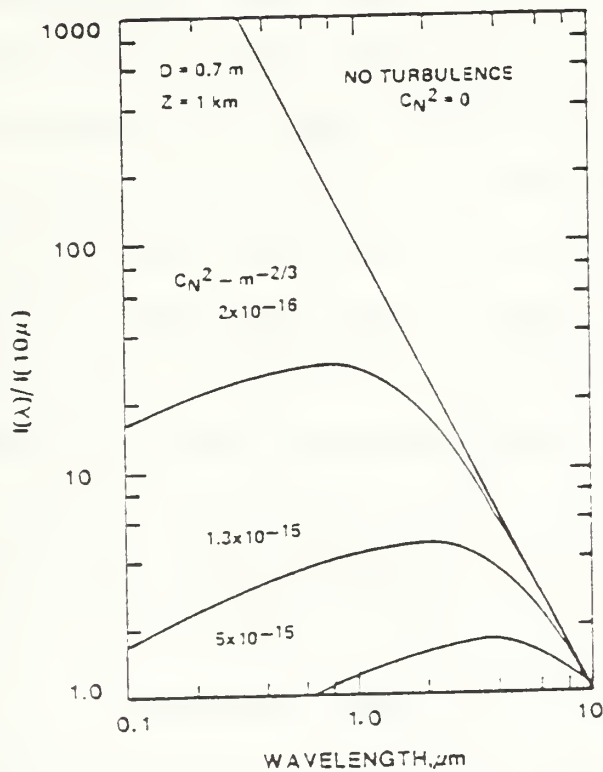


Figure 2-2: Dependence of turbulence effects on wavelength [3].

Thermal blooming or defocusing is a time dependent effect of absorption of a small amount of beam energy by the atmosphere along the beam path. The resultant rapid heating lowers the air density and also the refractive index, causing a nonlinear negative lens effect of divergence on the beam. Varying with atmospheric conditions, defocusing can occur in as little as 0.2s. This

length of time is crucial because it is close to a typical value of the "dwell time" necessary for a laser beam to remain focussed in order to damage or destroy a target. The spreading effect can dominate diffraction limited focusing. This can limit the irradiance on a target independent of the available power of the beam. Accounting for variable atmospheric velocity due to wind and the slew rate of a beam tracking a target, there will be a temperature gradient across the face of the beam, with the "cooler" air on the "upwind" side of the beam face, in the direction of the cumulative wind/slew velocity. The temperature gradient will result in a varying refractive index across the beam face, leading to an asymmetric distortion and growth of the beam cross section. With the "upwind" side of the beam face remaining at a lower average temperature, this side will tend to have a higher air density and thus a higher index of refraction. This causes the path of the defocused beam to bend "upwind" asymmetrically.

Peak irradiance on a target accounting for thermal bloom effects must be scaled by a factor of thermal distortion,  $N$ , which is a function of focusing of beam radii, the effects of a non-uniform velocity profile, and atmospheric attenuation,  $\alpha_T$ . The specific heat,  $c_p$ , of the air, the range,  $z$ , and the power,  $P$ , of the laser are also accounted for. Essentially,  $N \propto \alpha_T P_0 z / v D^3$ , where  $v$  is a wind velocity term,  $a_0$  is the collimated beam  $1/e$  radius, and  $D = 2\sqrt{2}a_0$  is the aperture diameter. An empirical relationship that works well in modeling systems evolves as  $I_{rel} = I_{bloom} / I_{peak} = 1 / (1 + 0.06N^2)$ . Since peak irradiance is proportional to the product of power and the empirical correction,  $I_{peak} \propto P \times I_{rel}$ , the peak irradiance on target will increase until  $I_{rel}$  decreases at a rate proportional to  $1/P$  or greater. This indicates that for a given beam size, focal range and atmospheric conditions, there exists a peak power,  $P_c$ , at which irradiance on target is maximum.



Using this empirical relationship, Fig 2-3 shows the effects of thermal blooming in limiting peak irradiance and maximum power for a propagating beam.

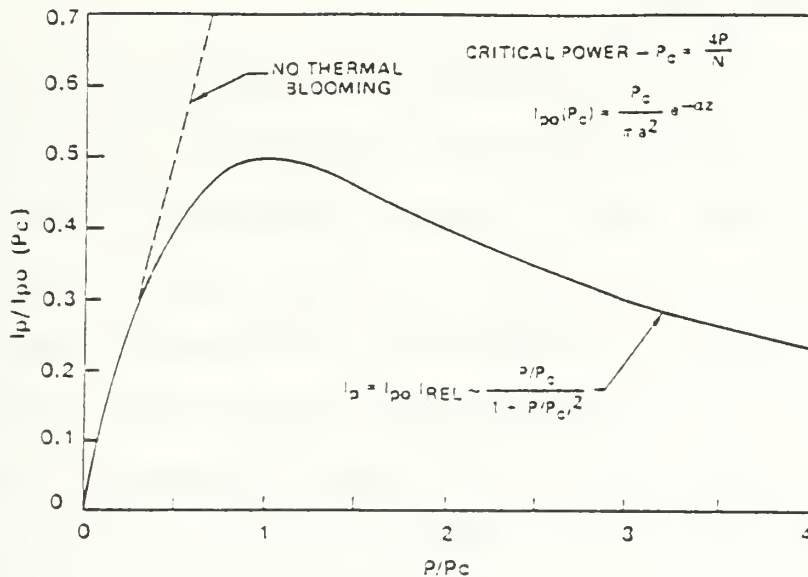


Figure 2-3: The normalized peak irradiance vs. the normalized power  $P/P_C$ , based on the empirical relationship of  $I_{bloom}/I_{peak}$  [3].

Unlike other atmospheric effects, increased power in the laser beam will not result in higher fluence on the target, but will only serve to further aggravate the blooming effect. This is a nonlinearity unlike any other atmospheric effect. All other phenomena result in increased target irradiation with higher power. Peak irradiance accounting for linear and nonlinear effects at range  $R = z$  is

$$I_P = \frac{P}{\pi a^2} \frac{\exp(-\alpha_T z)}{1 + 0.0625 N^2} \quad 2-5$$

The linear effects of diffraction, beam quality, jitter, and turbulence are accounted for by the rms beam radius

$$w^2 = \frac{2\beta^2\lambda^2 z^2}{\pi^2 D^2} + 2\langle\theta_x^2\rangle z^2 + 4(C_N^2 z)^{6/5}\lambda^{-2/5} z^2 \quad 2-6$$

where  $D = 2\sqrt{2}a_0$  is the aperture diameter, and the linear attenuation effects are covered by  $\alpha_T = \alpha_{abs} + \alpha_{scat}$ .

The effects of thermal blooming are time dependent, and so there is a difference between the propagation effects for continuous wave (cw) and pulsed beams. For a pulsed beam of diameter  $D$ , if the pulse repetition frequency (PRF) is less than the time needed for the cross wind,  $v_0$ , to clear the tube of atmosphere heated by the previous pulse, or  $PRF \leq v_0/D$ , there will be no thermal bloom effects from overlapping pulse beam effects. For time-scales outside of this regime, however, both pulsed and cw beams will experience bloom effects due to continuous heating. Through complex studies of various PRFs and beam face irradiance levels for pulsed beams, it has been found that pulsed beams are less affected by atmospheric effects than cw beams at long ranges [3].

Marine atmospheric propagation effects are difficult to predict on any useful time scale. The few controllable parameters include light wavelength and power level of the laser. Chemical HEL designs studied for naval application have all had basic flaws of limited fuel capacity and fixed wavelength. Free electron lasers, though less mature in design, have the valuable characteristics of tunable wavelength and manageable fuel and power requirements. The minimizing of atmospheric effects on laser beam propagation will need to be carried out not only by the selection of laser parameters, but also in creative beam optics. A system capable of atmospheric propagation diagnostics and

adaptation of deformable optics would greatly enhance the performance of any high-energy-laser weapon. Atmospheric diagnostics, hitherto the realm of astronomical studies for adaptive telescope optics, should be developed for inclusion into the control system of any SHEL design. In astronomy, optical system diagnostics are performed by observation of a "guide star" of known characteristics. For tactical military purposes, a low power laser carried by drone aircraft or other suitable platform could be aimed to illuminate diagnostic optics to allow analysis of the prevailing atmospheric conditions and subsequent optimization of the beam parameters and adaptive optics' adjustment [2,5].

A more exotic solution may be found by stationing a relay mirror system high above the FEL vessel aboard a long-endurance fixed-wing remotely-piloted vehicle (RPV) or balloon aircraft. A system centered on this concept, named Thunderball, was presented to the Physics department of the Naval Postgraduate School by Lieutenant Colonel Ed Pogue, USA, former Deputy Director of Directed Energy for the Strategic Defense Initiative Office. This concept had been studied by the Advanced Technology Group of W. J. Schafer Associates [6]. The chief advantages of this system, whose aircraft would be stationed at altitudes approaching eighty thousand feet, would be the minimization of distance traveled through the dense lower atmosphere. This would help minimize the most harmful effects of the atmosphere. Additionally a beam of greater diameter, and thus lower power density across the beam face, could be used. This would lessen the damaging effects of atmospheric influences. Once the beam reached the optical system aboard the aircraft, a beam cleanup and refocusing system could narrow and redirect the beam toward a target far beyond the horizon of the FEL vessel below. This system would be well suited for a defensive mission against incoming ballistic missiles.

### III. FREE ELECTRON LASER THEORY

#### A. BASIC FREE ELECTRON LASER PHYSICS

Free electron laser systems consist of four basic components, the electron beam accelerator, the optics which include the beam transport system and the FEL undulator and resonator. The accelerator produces a stream of relativistic electrons that is injected into the periodic magnetic field of the FEL undulator, which "wiggles" the electrons along sinusoidal trajectories. The periodic transverse acceleration of the highly relativistic electrons results in classical synchrotron radiation into a forward cone along the beam path. The resonator cavity consists of two curved mirrors, one is fully reflecting and one is partially reflecting, placed beyond the ends of the axis of the undulator. The mirrors are designed to sustain a transverse Gaussian mode shape. The total resonator length is typically  $S \approx 5 - 20\text{m}$ . The FEL oscillator starts from spontaneous emission, some of which is saved in the resonating cavity resulting in an increase in optical power. Repeated coupling of the electrons with the optical and undulator fields results in the bunching of the electrons. This amplifies the amplitude of the wavefront, resulting in coherent radiation and lasing. Undulator gain is the fractional change in optical power per pass,  $G = \Delta P/P$ . Typical values for  $G \approx 0.10$  for a low gain FEL and  $G \approx 10^4$  for a high gain FEL.

The bunching effect is crucial to FEL operation, and is highly dependent on the quality of the electron beam produced by the electron accelerator. Specifically, the energy spread of the electrons as well as the angular spread of the beam must be reasonably low for FEL success, the energy spread among



the electrons in the beam results in differences of velocity within the undulator, leading to an axial smearing of the electron bunch entering the undulator. If the velocity differences spreads the electrons beyond the optical wavelength,  $\lambda$ , the FEL gain would be seriously degraded. Variations of the electron injection angle, or angular spread, results in non-axial components of bunch velocity. Reducing the axial velocity will also serve to degrade gain in much the same way as an energy spread.

Emittance and beam spreading, collectively known as "beam quality," influence bunching effects. Emittance,  $\varepsilon = r \bar{\theta}$ , is the product of the root-mean-square (rms) values of radial and angular spreads of the electron beam. In the tuning of a given electron transport system, both of these parameters may be changed, but their product,  $\varepsilon = r \bar{\theta}$ , remains constant. The normalized emittance,  $\varepsilon_n = \gamma \varepsilon$ , is the product of the electron beam Lorentz factor,  $\gamma$ , and the emittance  $\varepsilon$ . The normalized emittance tends to remain constant even when the electron beam is accelerated to higher energies. Normalized emittances typically vary from a few tens to a hundred mm-mrad.

The accelerator produces relativistic bunches of electrons with peak currents from 1 A to 1kA, and bunch lengths of  $l_b \approx 10^{-1}\text{cm}$ . The relativistic electron beam will typically have a Lorentz factor,  $\gamma$ , from ten to the low hundreds. Typical electron beam radii are  $r_b \approx 0.10\text{cm}$ . These result in electron densities of  $\rho \approx 10^{12}\text{cm}^{-3}$  to  $10^{13}\text{cm}^{-3}$ . With Lorentz factors  $\gamma$  varying from ten a few hundred, the beam energies,  $(\gamma - 1)mc^2$ , range from several tens of to hundreds of MeV, where  $m$  is the electron mass,  $c$  is the speed of light, and  $mc^2 = 0.511\text{MeV}$  is the electron rest mass.

The undulator consists of a series of alternating magnetic pole pieces forming an intense magnetic field that accelerates the relativistic electron beam into periodic transverse motion. Within the undulator, electron bunches undergo one cycle along an axial length known as an undulator wavelength,  $\lambda_0$ , which is typically five to ten cm. The number of undulator wavelengths,  $N$ , varies from twenty five to 250, which results in undulator length  $L = N\lambda_0$  from one to ten meters. The undulator magnetic field strength,  $B$ , ranges from 3kG to 5kG. Mean undulator magnetic field strength,  $\bar{B}$ , is rms field averaged over the undulator period  $\lambda_0$ . For helically (circularly) polarized undulators,  $\bar{B} = B$ , due to the constant acceleration of the electrons in a helical path along the axis of the undulator. Helical undulators produce circularly-polarized radiation. Magnetic fields for linearly-polarized undulators result in non-constant acceleration due to the sinusoidal electron path, so that  $\bar{B} = B/\sqrt{2}$ . Linearly-polarized undulators produce linearly-polarized radiation.

These parameters, with the electron charge magnitude,  $e$ , combine as the "undulator parameter" [7],

$$K = \frac{e\bar{B}\lambda_0}{2\pi mc^2}.$$

The undulator parameter,  $K$  varies from 0.1 to 3.  $K$  may be varied by altering the separation distance between pole faces along the undulator in order to change  $\bar{B}$ . The optical radiation wavelength,  $\lambda$ , produced by the FEL is given by [7]

$$\lambda \approx \left\{ \frac{1 + K^2}{2\gamma^2} \right\} \lambda_0.$$

The optical wavelength is a function of the undulator magnetic field and the

electron energy from the accelerator, as represented by the Lorentz factor  $\gamma$ . This relation reflects the tunability of the FEL over a very broad range of wavelengths. Experiments have a  $\times 10$  range of tunability, and the FEL can operate from the mm to the X-Ray wavelength range.

Short optical wavelengths are a result of the Doppler shift effect on the undulator and optical radiation fields as "seen" by the highly relativistic electrons. The electrons "see" a Lorentz contracted undulator wavelength,  $\lambda_0' \approx \lambda_0 / \gamma$ . The electrons emit light at a longer Doppler shifted wavelength  $\lambda' \approx 2\gamma\lambda$ . With the similarity of the Doppler shifted light and the Lorentz contracted undulator wavelength,  $\lambda' \approx \lambda_0'$ , the relationship of the radiation wavelength to the undulator wavelength becomes  $\lambda \approx \lambda_0 / 2\gamma^2$ . This is the mechanism which enables short wavelengths to be produced.

The resonance condition is met when one wavelength of light passes over an electron as the electron traverses through the length of one undulator wavelength. As the electron bunch is subjected to the resonant forces of the combined undulator and optical fields, the electrons undergo either stimulated emission or absorption, depending on the phase relationship of the bunch relative to the optical field. This new light from the electrons will interfere with the light of the optical mode. If the net interaction of the radiation is constructive interference, there exists a regime of positive gain,  $G = \Delta P / P > 0$ , for the undulator.

Figure 3-1 illustrates the interaction of an electron with the optical mode and magnetic fields within the undulator. The top diagram shows an electron bunch and an optical pulse in the undulator. The middle diagram illustrates the details along one undulator period.

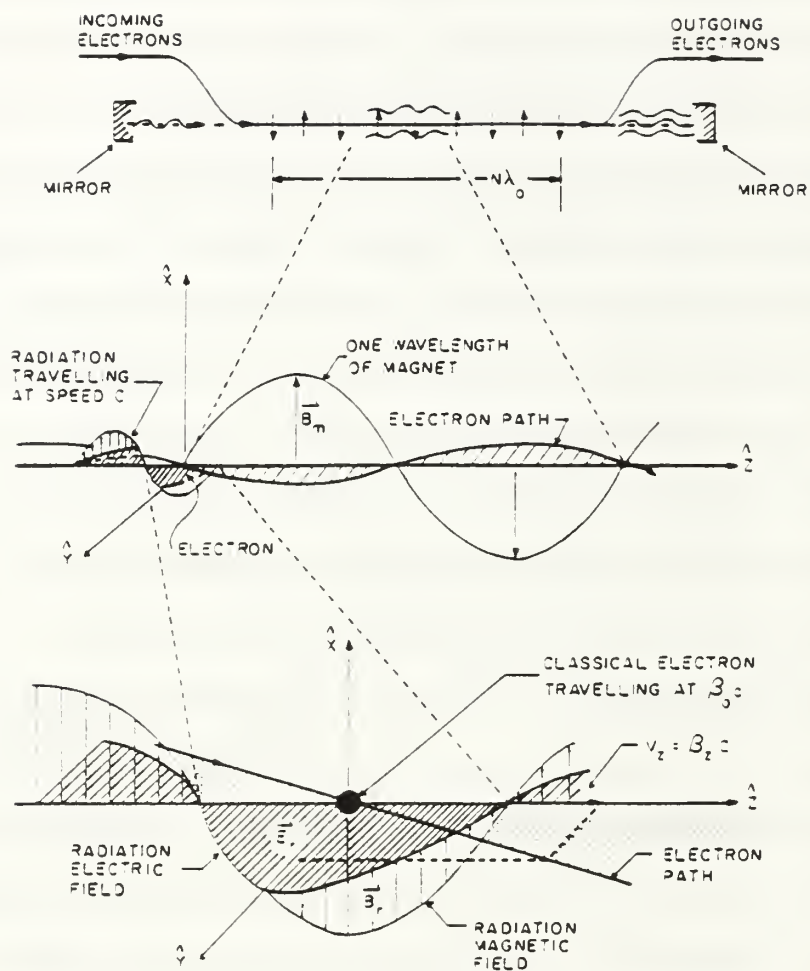


Figure 3-1: Fundamental design and electron-optical mode interactions within the undulator of an FEL.



The electrons follow a sinusoidal trajectory along the periodic magnetic undulator field while one wavelength of light passes over each electron. The bottom diagram details the electron-optical mode interaction. Depending on the relative phase between the optical mode and the electron, the electron will be subject to either a retarding or accelerating force that will induce it to either emit or absorb energy. Conservation of energy determines that the energy transferred from the electrons must be absorbed by the optical mode wave. This results in optical amplitude growth and FEL gain. Should the phase relationship cause the electron to be accelerated, the force to do so will rob the optical mode of energy and result in decreased amplitude, or negative FEL gain. In non-resonant systems, gain can be positive or negative in various positions along the undulator resulting in complex optical amplitude profiles.

## B. ELECTRON DYNAMICS

The highly relativistic electron beam is subject to the combined forces of the radiation of the optical mode and the magnetic field of the undulator. The equations of the Lorentz force exerted on the electrons are

$$\vec{F} = \frac{d}{dt}(\gamma mc \vec{\beta}) = -e [\vec{E} + (\vec{\beta} \times \vec{B})], \quad \frac{d}{dt}(\gamma mc^2) = -ec(\vec{\beta} \cdot \vec{E}) \quad 3-1$$

where  $\vec{\beta} = \vec{v}/c$  is the ratio of electron velocity  $\vec{v}$  to the speed of light  $c$ ,  $\vec{E}$  is the optical electric field, and the net magnetic field,  $\vec{B} = \vec{B}_r + \vec{B}_u$  is the sum of the magnetic fields of the optical mode and the helical undulator [7]. Using the combined undulator and optical fields in 3-1, and integrating over time, the transverse electron motion within the undulator may be solved. There are a total of five equations in 3-1, with only four unknown terms  $[\vec{x}(t), \gamma(t)]$ , so that one of the five equations may be disregarded. The relativistic electrons have

an initial position  $z_0$ , an axial velocity  $v_z = \beta_z c$ , where  $\beta_z = 1 - (1 + K^2)/\gamma^2 \approx 1$ , and the position along the undulator axis is given by  $z(t) \approx z_0 + \beta_z ct + \dots$ . The transverse velocity  $\beta_\perp = \sqrt{1 - \beta_z^2} \ll 1$ , so the magnitude of the transverse motion of the electrons is much less than the axial motion. The transverse undulator fields are much greater than the transverse optical fields, so that the transverse force equation of the electrons becomes

$$\vec{F}_\perp = \frac{d}{dt}(\gamma \beta_\perp) \approx \frac{-e}{mc} \beta_z B [-\sin(k_0 z), \cos(k_0 z), 0]. \quad 3-2$$

Where  $k_0 = 2\pi/\lambda_0$  is the undulator wave number. Integrating this equation over time, and assuming perfect beam injection, yields the transverse velocity:

$$\vec{\beta}_\perp = \frac{-K}{\gamma} [\cos(k_0 z), \sin(k_0 z), 0]. \quad 3-3$$

One more integration will result in the transverse position relationship for the electrons:

$$X_\perp = \frac{-K}{\gamma k_0} \approx \frac{K\lambda_0}{2\pi\gamma} [\sin(k_0 z), -\cos(k_0 z), 0].$$

It can easily be seen here that because  $K \approx 1$  and the Lorentz factor  $\gamma \approx 100$  that the magnitude of the transverse motion is relatively small.

### C. ENERGY EVOLUTION

The second term in the Lorentz force equations 3-1 determines the evolution of the energy. Using the expression above for transverse velocity  $\beta_\perp$  3-3, the approximate electron position  $z = z_0 + \beta_0 ct + \dots$ , for Lorentz factor  $\gamma \gg 1$ , the energy for a weak field regime may be approximately calculated. The optical electric field is

$$\vec{E}_r = E (\cos(kz - \omega t), -\sin(kz - \omega t), 0),$$

where the wave number is given by  $k = 2\pi/\lambda$ , and the principle carrier frequency is given by  $\omega = kc = 2\pi c/\lambda$ . Using  $\dot{\gamma} = -e(\vec{\beta} \cdot \vec{E})/mc$ , the initial position  $z_0 = z_0 + \beta_0 ct$ , and substituting the expression for  $\vec{E}_r$ , the energy term evolves as

$$\dot{\gamma} = \frac{eKE}{\gamma mc} \cos((k + k_0)z - \omega t) \approx \frac{eKE}{\gamma mc} \cos((k + k_0)z_0 + [(k + k_0)\beta_0 - k]ct), \quad 3-4$$

where  $\beta_0$  is the ratio of initial electron velocity  $v_0$  and the speed of light  $c$  [8]. Define the initial phase as  $\zeta_0 = (k_0 + k)z_0 \approx 2\pi z_0/\lambda$ , which relates the initial electron  $z$  position relative to the optical wave. The time dependent phase is  $\zeta(\tau) = (k_0 + k)z(t) - \omega t$ . Electrons separated by  $\Delta\zeta = 2\pi$  are in identical positions in adjacent optical wavelengths. The phase velocity is  $v_0 = L[(k_0 + k)\beta_0 - k]$ , and the dimensionless time is  $\tau = ct/L$ . The energy evolution may now be written as  $\dot{\gamma} = (eKE/\gamma mc)\cos(\zeta_0 + v_0\tau)$ . This can also be restated in a dimensionless time regime where  $(\dots)$  represents a dimensionless time derivative  $d(\dots)/d\tau$ , so that  $\dot{\gamma} = (eEKL/\gamma mc^2)\cos(\zeta_0 + v_0\tau)$ . Integration of this term will result in

$$\gamma = \gamma_0 + \frac{eKEL}{\gamma_0 mc^2 v_0} [\sin(\zeta_0 + v_0\tau) - \sin(\zeta_0)],$$

where  $\gamma_0$  is the initial energy. Rearranging, the time varying energy in the weak optical field regime is

$$\gamma(\tau) = \gamma_0 + \frac{A}{v_0} [\sin(\zeta_0 + v_0\tau) - \sin(\zeta_0)],$$

where the term  $A = eEKL/\gamma_0 mc^2$  determines the energy exchange. This shows that the energy exchange of an FEL is controlled by the initial energy  $\gamma_0$  of the

electrons, the magnitude of the electric field  $E$ , the magnetic field strength  $K \propto B$ , and the electron phase  $\zeta_0 \approx 2\pi z_0/\lambda$  within each optical wavelength, and the electron phase velocity  $v_0$ . For large  $v_0 (v_0 \gg \pi)$  the change in electron energy oscillates rapidly along the undulator and is small. For  $v_0$  near resonance ( $v_0 \approx 0$ ), the electron energy changes are linear in  $\tau$ ,  $\gamma(\tau) \approx \gamma_0 + A\tau \cos(\zeta_0)$ , and are periodic in the electron phase  $\zeta_0$ . For  $-\pi/2 < \zeta_0 < \pi/2$ , the electron energy increases, and for  $\pi/2 < \zeta_0 < 3\pi/2$ , the electron energy decreases. For the whole beam randomly spread in  $\zeta_0$ , the average energy change is zero. To this order in the field  $E$ , there is no gain.

#### D. THE PENDULUM EQUATION

The FEL phase and phase velocity relationship may be calculated by returning to the Lorentz energy expression,  $\dot{\gamma} = -(e/mc) \vec{\beta}_\perp \cdot \vec{E}_r$ . FEL gain is the net energy exchange to the optical field and must be calculated to higher order in the field  $E$ . Substitution of the optical mode electric field into 3-4 results in an expression of energy gain [8]

$$\frac{\dot{\gamma}}{\gamma} = \frac{eKEL}{\gamma^2 mc} \cos(\zeta + \phi).$$

To track the electron phase changes as the energy changes, the Lorentz factor is rewritten  $\gamma^{-2} = 1 - \vec{\beta}^2 = 1 - (\beta_\perp^2 + \beta_z^2)$  where  $\beta_\perp \approx K/\gamma$ . For highly relativistic electrons  $\gamma \gg 1$ , and  $\beta_z \approx 1 - (1 + K^2)\gamma^{-2}$ . Phase velocity  $\dot{\zeta} = v = (k_0 + k)\dot{z} - \omega$ , and the second derivative of phase, the rate of phase velocity change, is

$$\ddot{\zeta} = \dot{v} = (k_0 + k)\ddot{z} \approx kc \left\{ \frac{1 + K^2}{\gamma^2} \right\} \frac{\dot{\gamma}}{\gamma} \approx kc \left\{ \frac{1 + K^2}{\gamma^2} \right\} \frac{eKE}{\gamma^2 mc} \cos(\zeta + \phi). \quad 3-5$$

Equation 3-5 has the form of the Pendulum equation. Taking advantage of the



fact that the initial carrier frequency  $\omega_0 = k_0 c = \omega (1 + K^2)/2\gamma^2$ , 3-5 can be restated as

$$\ddot{\zeta} = \frac{2eKEk_0}{\gamma^2 m} \cos(\zeta + \phi).$$

The dimensionless time  $\tau = ct/L$ , wherein  $0 \leq \tau \leq 1$  as the electrons travel down the axis of the undulator, may be inserted into these expressions. This requires that  $d(..)/dt = L/c \, d(..)/d\tau$  or  $(..)$  becomes  $(\overset{\circ}{..})$ , and  $d^2(..)/dt^2 = (L/c)^2 \, d^2(..)/d\tau^2 = (\overset{\circ\circ}{..})$ . This now allows the Pendulum equation, 3-5 be rewritten:

$$\overset{\circ\circ}{\zeta}(\tau) = \overset{\circ}{v} = \left\{ \frac{L}{c} \right\}^2 \frac{2eEKk_0}{\gamma_0^2 m} \cos(\zeta + \phi) = |a| \cos(\zeta + \phi), \quad 3-6$$

where the dimensionless term  $|a| = 4\pi NeKEL/\gamma_0^2 mc^2$  is the strength or magnitude of the optical field for a circularly-polarized undulator [9].  $|a|$  shows that higher velocity (larger  $\gamma$ ) electrons would require a stronger optical field  $E$  in order to achieve the same electron bunching. When  $|a| \ll \pi$  the field is considered to be in a "weak field" regime, and the electron bunching after a single pass through the undulator is negligible. When  $|a| \approx \pi$  the bunching effect becomes noticeable. While  $|a| \gg \pi$  is the "strong field" case, where the electrons quickly bunch within the undulator and may cause the onset of "trapped particle instability." If the optical power is strong enough to cause one synchrotron oscillation for each pass, the electrons become trapped in deep potential wells. This results in beam current oscillation that destabilizes the carrier wave, causing sideband frequencies to grow. The coherent wave that had been established by the FEL interaction, may be amplified or degraded by the oscillating current of the trapped electrons. [9]

## E. THE WAVE EQUATION

The FEL oscillator starts with spontaneous emission and creates a classical light wave that is amplified by stimulated emission. Because the spontaneous emission bandwidth of the wave is approximately  $1/N$ , where  $N$  is the number of periods in the undulator, there is some measure of coherence in the initial light wave. Since  $N \gg 1$ , the bandwidth is sufficiently narrow to form a classical wave with a complex field envelope  $(E(z,t), \phi(z,t))$  whose circularly-polarized electric and magnetic fields are expressed by

$$\vec{E}_r(\vec{r}, t) = E(z, t)[\cos(\psi), -\sin(\psi), 0], \quad \vec{B}_r(\vec{r}, t) = E(z, t)[\sin(\psi), \cos(\psi), 0] \quad 3-7$$

where  $E(z, t)$  is the wave amplitude,  $\psi = kz - \omega t + \phi(z, t)$ , and the phase is  $\phi(z, t)$ . The amplitude and phase vary slowly in time over the optical period ( $\dot{E} \ll \omega E, \dot{\phi} \ll \omega \phi$ ), and also in space over the length of an optical wavelength  $\lambda$ , such that ( $\dot{E} \ll kE, \dot{\phi} \ll k\phi$ ) where  $k = 2\pi/\lambda$  [8]. This approximation allows the fields to be derived from the vector potential [9]:

$$\vec{A}(\vec{r}, t) = \frac{E(z, t)}{k} [\sin(\psi), \cos(\psi), 0].$$

The optical wave equation becomes

$$\begin{aligned} \square^2 \vec{A}(\vec{r}, t) &= 2 \left[ \frac{\partial E}{\partial z} + \frac{1}{c} \frac{\partial E}{\partial t} \right] [\cos(\psi), -\sin(\psi), 0] + 2E \left[ \frac{\partial \phi}{\partial z} + \frac{1}{c} \frac{\partial \phi}{\partial t} \right] [-\sin(\psi), -\cos(\psi), 0] \\ &\approx \frac{-4\pi}{c} \vec{J}_\perp(\vec{r}, t), \end{aligned} \quad 3-8$$

where  $\square^2 = (\nabla^2 - (1/c^2) (\partial^2/\partial t^2))$  is the D'Alembertian operator, and  $\vec{J}_\perp$  is the transverse beam current. If there is no  $\vec{J}_\perp$  (no transverse motion of the electrons), then the solution to 3-7 is  $E = E(z-ct)$  and  $\phi = \phi(z-ct)$ .

Each electron contributes to the total transverse current so that

$$\vec{J}_\perp = -ec \sum_i \vec{\beta}_\perp \delta^{(3)}(\vec{x} - \vec{r}_i), \quad 3-9$$

where  $\vec{r}_i$  is the trajectory of the  $i^{th}$  electron and  $\delta^{(3)}$  is a 3 dimensional Dirac Delta Function [8]. The coherence volume,  $V_c$ , is the product of the gain bandwidth length,  $N\lambda$ , and the transverse mode area,  $\lambda L = \lambda N\lambda_0$ , so that  $V_c = N^2\lambda^2\lambda_0$ . In order to correct for the fast variation of the trigonometric functions of  $\psi$  in 3-7, an average is taken over a small volume element  $dV_c$  which is small relative to the coherence volume, but large relative to an optical wavelength  $\lambda$ . [9] Using this averaging and inserting 3-7, 3-8 becomes

$$\left[ \frac{\partial}{\partial z} + \frac{1}{c} \frac{\partial}{\partial t} \right] E e^{i\phi} = -4\pi e K \rho(z - \beta_z ct) \langle e^{-i\zeta} \gamma \rangle \quad 3-10$$

where  $\rho(z - \beta_z ct)$  is the mean density of the electron bunch. If the longitudinal spread of the bunch is so great that the density is no longer a function of axial position, there will be uniform evolution of the electron pulse along its length, and no optical modes are followed, so that 3-10 is no longer dependent on  $z$ . If the number of undulator periods  $N$  is large, there is a small bandwidth and  $\gamma$  changes only slightly, and the wave equation becomes

$$\ddot{a} = -j \langle e^{-i\zeta} \rangle \quad 3-11$$

where

$$a = \frac{4\pi N e K E L e^{i\phi}}{\gamma^2 m c^2}, \quad j = \frac{8N(e\pi K L)^2 \rho}{\gamma^3 m c^2}$$

The field magnitude is  $a$ , and  $j$  is the dimensionless beam current [8,9]. The beam current,  $j$ , determines the reaction of the optical mode to the bunching of the electron beam, and provides coupling between the wave and the electron

beam. When  $j \leq \pi$  the gain is low, and when  $j \gg \pi$  the gain is high.

For a linearly-polarized undulator, the non-uniformity of electron acceleration requires that these expressions be modified by  $K \rightarrow K(J_0(\xi) - J_1(\xi))$ . Here  $K$  is the undulator parameter,  $\xi = K^2/2(1 + K^2)$ , and  $J_0$  and  $J_1$  are Bessel functions of the first and second kind. [9]

## F. DIMENSIONLESS PARAMETERS

Certain dimensionless parameters recur throughout the descriptions of the physics of the FEL. Their use allows quick summarization of performance without regression to involved calculations. Several important dimensionless parameters have already been defined and are used in this paper. They include the undulator parameter,  $K$ , the electron phase and phase velocity  $\zeta$  and  $v$ , the beam current  $j$ , and the optical field magnitude  $|a|$ . In the derivation of 3-10, it has been assumed that electron and optical mode sizes are the same. The filling factor  $F = \pi r_e^2 / \pi W_0^2$  is the ratio of the area of the electron beam to that of the optical mode waist. When the electron beam is entirely within the optical mode, the dimensionless beam current  $j$  (3-10) should also include the filling factor  $F$  as a correction for the smaller volume of the electron beam.

The transverse dimensions can be normalized by the optical mode radius  $\sqrt{\pi/L\lambda}$ . Macroscopic longitudinal dimensions can be normalized by the undulator length  $L$ . The normalized electron pulse length is  $\sigma_z = l_e / N\lambda$  where  $l_e$  is the electron bunch length. The Rayleigh length  $Z_0$  is a measure of optical diffraction properties and is dependent on optical wavelength, mirror design and configuration. The normalized Rayleigh length is  $z_0 = Z_0 / L$ .  $Z_0$  is related to the

optical mode waist radius,  $W_0$ , by  $Z_0 = \pi W_0^2 / \lambda$ . The normalized mode waist radius,  $w_0 = W_0 \sqrt{\pi L / \lambda}$ , is related to the normalized Rayleigh length by  $w_0 = W_0 \sqrt{\pi L / \lambda} = \sqrt{\lambda Z_0 / \pi} \sqrt{\pi L / \lambda} = \sqrt{Z_0}$ .

The slippage distance  $\Delta s$  is the difference in distances traveled by the optical wave and the electron beam as they move down the undulator. This is also the length that the light moving at  $c$  passes over the slower electrons moving at  $\beta_z c$  during this period. Their relative speed,  $\Delta v = (1 - \beta_z)c$ , multiplied by the period of one undulator pass  $\Delta t = L/c$ , is the slippage distance  $\Delta s = \Delta v \Delta t = (1 - \beta_z)c(L/c) = (1 - \beta_z)L$ . Inserting the definition of  $\beta_z$ , undulator length  $L = N\lambda_0$ , and wavelength  $\lambda = \lambda_0(1 + K^2)/2\gamma^2$ , the expression for slippage distance becomes  $\Delta s \approx N\lambda$ . The normalized electron pulse length  $\sigma_z = l_e/N\lambda$  is scaled by the slippage distance [9].



## IV. THE CEBAF INFRARED FEL DESIGN

### A. BACKGROUND

The Continuous Electron Beam Accelerator Facility (CEBAF) in Newport News Va. is administered by the Southeastern Universities Research Association (SURA) for application to nuclear science, technology and industry. The CEBAF superconducting accelerator incorporates two 400 MeV linear accelerators (linacs) with interconnecting, recirculating electron beam lines. These will allow five simultaneous electron beams at energies between 800 MeV and 4 GeV to be delivered to three end-stations. A program is underway to design and construct two high power FELs operating at the near infrared (IR) and the deep ultraviolet (UV) wavelengths. The design configuration of the FEL facility will allow laser operation without interference to the nuclear science research. The IR FEL will take advantage of the operational 45 MeV accelerator injector as its driver, while the UV FEL will use the 400 MeV North Linac. [10]

The CEBAF facility has several features which make it interesting for FELs. The CEBAF linacs will supply the FELs with a high-quality electron beam with normalized emittance  $\epsilon_n = 15$  mm-mrad, a high average power of 800 kW, energy spread  $\Delta\gamma/\gamma = .001$ , and a duty cycle of 100 %. The fraction of energy extracted by the FEL is  $1/N$ , so that the average power of the FEL would be  $\approx 30$  kW.

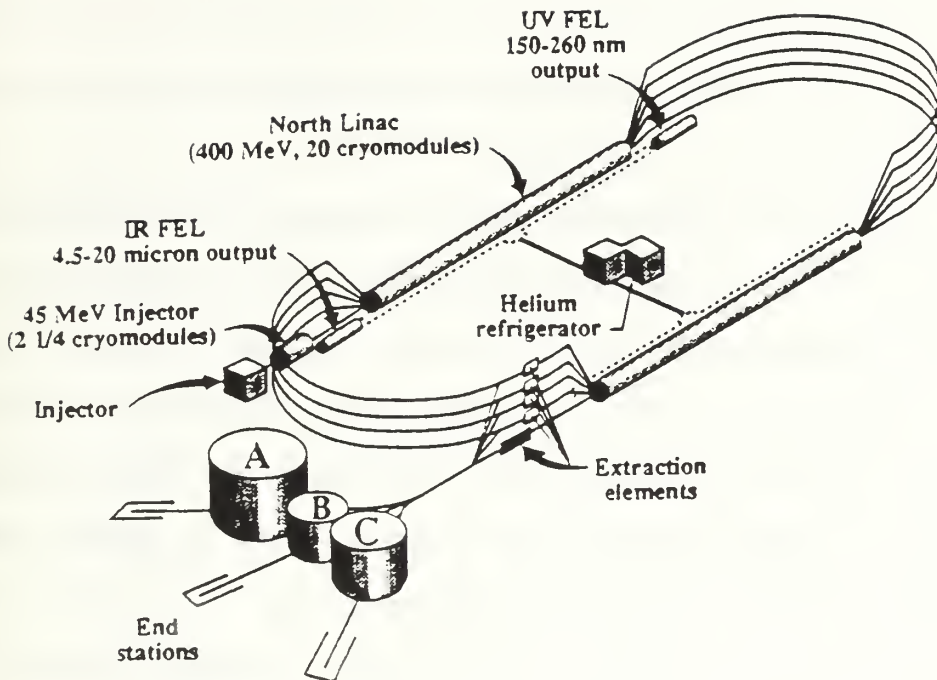


Figure 4-1: CEBAF IR and UV FEL configuration. The UV FEL will utilize the 400 MeV North Linac for its driver, while the IR FEL will use the 45 MeV Injector [10].

These are important parameters because if the FEL were ever to be developed for military use, high average power and performance goals would have to be achieved, and this experiment will be an important step. Additionally, the accelerator uses advanced superconducting technology that will be incorporated into the next generation of all-electric drive naval vessels that are now being planned.

The Infrared (IR) FEL is a multi-pass, high-power laser operating in the near infrared at a nominal wavelength of  $\lambda \approx 15\mu\text{m}$  and micropulse frequency of 7.5 MHz [1]. The peak current is 72 A with a short micropulse length of  $l_p \approx 0.05$  cm. The electron beam energy is  $(\gamma-1)mc^2 = 45$  MeV where the

Lorentz factor is  $\gamma = 89$ , the electron mass is  $m$ , and  $c$  is the speed of light. The high-quality electron beam has energy spread of only  $\Delta\gamma/\gamma = 0.001$  with a normalized emittance of  $\epsilon_n = \gamma \epsilon \approx 15$  mm-mrad. [11]

An FEL with a high-quality electron beam operating at IR wavelengths tends to have an electron beam that is much smaller than the optical mode in the transverse dimension, and smaller than the slippage distance in the longitudinal dimension. The optical mode waist radius is proportional to  $\lambda^{1/2}$ , and the slippage distance is proportional to  $\lambda$ . In the transverse direction, mode distortion tends to increase the gain, while in the longitudinal direction, the short-pulse slippage effects tend to decrease the gain. [11]

In the CEBAF case, the electron beam radius is  $r_e \approx 0.03$  cm, and is much smaller than the radius of the optical mode,  $W_0 \approx 0.15$  cm. Simple theory indicates gain is proportional to the product of filling factor  $F$  and dimensionless beam current  $j$ , but the actual gain observed in simulations is found to be a function of filling factor  $F$ . [10,11]

## B. CEBAF IR FEL PARAMETERS

The length of the proposed linearly-polarized undulator is  $L = 1.5$  m with wavelength of  $\lambda_0 = 6$  cm over  $N = 25$  periods. The linearly-polarized undulator peak field strength is  $B = 4.4$  kG, giving an undulator parameter of  $K = eB\lambda_0/2\sqrt{2}\pi mc^2 \approx 1.76$ . A non-focussed electron beam with smooth propagation and minimum electron phase velocity spread is desirable for injection into the undulator field. This requires a matching condition between the rms radial beam spread,  $\tau$ , and the rms angular spread  $\bar{\theta}$ , such that  $Kk_0\tau = \sqrt{2}\gamma\bar{\theta}$  [9]. The emittance is  $\epsilon = \tau\bar{\theta}$ , so that the matched electron beam

radius is then  $r_e = (\gamma\epsilon\lambda_0/\sqrt{2\pi}K)^{1/2} \approx 0.03$  cm. The off-axis injection caused by the radial and axial spreads, and the off-axis focusing fields cause a slow, transverse "betatron" oscillation of the electrons, with  $NK/\gamma \approx 0.5$  betatron oscillations along the undulator [9]. The amplitude of the electron's transverse wiggling motion is  $\Delta x \approx K\lambda_0/\sqrt{2\pi}\gamma \approx 0.03$  cm, and is comparable to the size of the electron beam. The nominal resonant wavelength is  $\lambda = \lambda_0(1+K^2)/2\gamma^2 \approx 15$   $\mu\text{m}$ , but the CEBAF IR FEL will be tunable from 5 $\mu\text{m}$  to 20 $\mu\text{m}$ . The dimensionless electron beam current  $j = 8N[\pi eKLJJ]^2\rho/\gamma^3mc^2 \approx 138$ , where  $\rho \approx 4 \times 10^{12}$   $\text{cm}^{-3}$  is the electron particle density, and the Bessel function factors,  $JJ = J_0(\xi) - J_1(\xi) \approx 0.78$  with  $\xi = K^2/(2(1+K^2)) \approx 0.38$ , describe the reduced coupling in a linearly-polarized undulator. [11]

The value of the Rayleigh length that minimizes the optical mode volume is  $Z_0 = L/\sqrt{12} \approx 43$  cm [9]. Assuming the optical mode is shaped as a lowest-order Gaussian with its waist at the center of the undulator ( $\tau_w = 0.5$ ), the filling factor averaged along the undulator's length is  $F = r_e^2/[W_0^2(1+L^2/12Z_0^2)] \approx 0.027$  where the area of the optical mode waist is  $\pi W_0^2 = Z_0\lambda$  [9]. The theoretical single-mode gain is given by  $G_0 \approx 0.135jF \approx 50$  % [12], and does not include the effects of beam quality, self-consistent field growth, short-pulses, or optical diffraction. When the interaction includes self-consistent growth of the optical field, the gain increases to  $G \approx 57$  %. The electron beam energy spread has the minor effect of reducing the gain by only 0.5 %, and the effect of emittance is even smaller. The CEBAF IR FEL electron beam is of such high quality, we will not include the effects in further simulations. [11]

### C. SHORT-PULSE EFFECTS

When the length of the electron pulse,  $l_e$ , is comparable to the slippage distance,  $\Delta s \approx N\lambda$ , the Fourier components of the pulse current are comparable to the gain bandwidth, and short-pulse effects influence the interactions in the undulator [9]. As an optical pulse bounces off the resonator mirrors and arrives at the entrance to the undulator, at  $\tau = 0$ , an electron micropulse from the accelerator is timed to arrive simultaneously. A slight displacement of one of the resonator mirrors, termed the "desynchronism"  $d = \Delta s/n\lambda$ , alters the distance the rebounding light must travel, and therefore will serve as a means to adjust the arrival of the optical pulse relative to the subsequent electron pulses. Desynchronism,  $d$ , is normalized to the slippage distance, and an exact synchronism between arrivals of the light and the electron pulses occurs when  $d = 0$ .

For the CEBAF IR FEL operating at the nominal wavelength  $\lambda = 15\mu\text{m}$ , Figure 4-2 shows an undulator with exact synchronism  $d=0$ . The window for calculation, at middle left, is four slippage distances long, and travels with the light pulse at speed  $c$ . The electron pulse, traveling at slower speed  $\beta_z c$ , slips backward through one-fourth of the window per pass. The positions of the short electron pulse relative to the optical pulse is shown at left bottom. The electron pulse position  $j(z-\tau)$ , initially is shown as the lighter parabolic shape at  $\tau = 0$ . As bunching develops the electron pulse slips backward, and the final position is indicated by the darker shape at  $\tau = 1$ . The pulse form is parabolic shape  $j(z) = j(1-2z^2/\sigma_z^2)$  for  $j(z)>0$ , or otherwise zero. The electron normalized pulse length  $\sigma_z = l_e/N\lambda = 1.4$ , and the peak current is  $jF = 3.8$  where  $F = 0.027$ . The optical amplitude grows proportionally to  $j$  on each pass, while amplitude losses due to the resonator are calculated by  $e^{-1/Q}$  for each pass. [9,11]



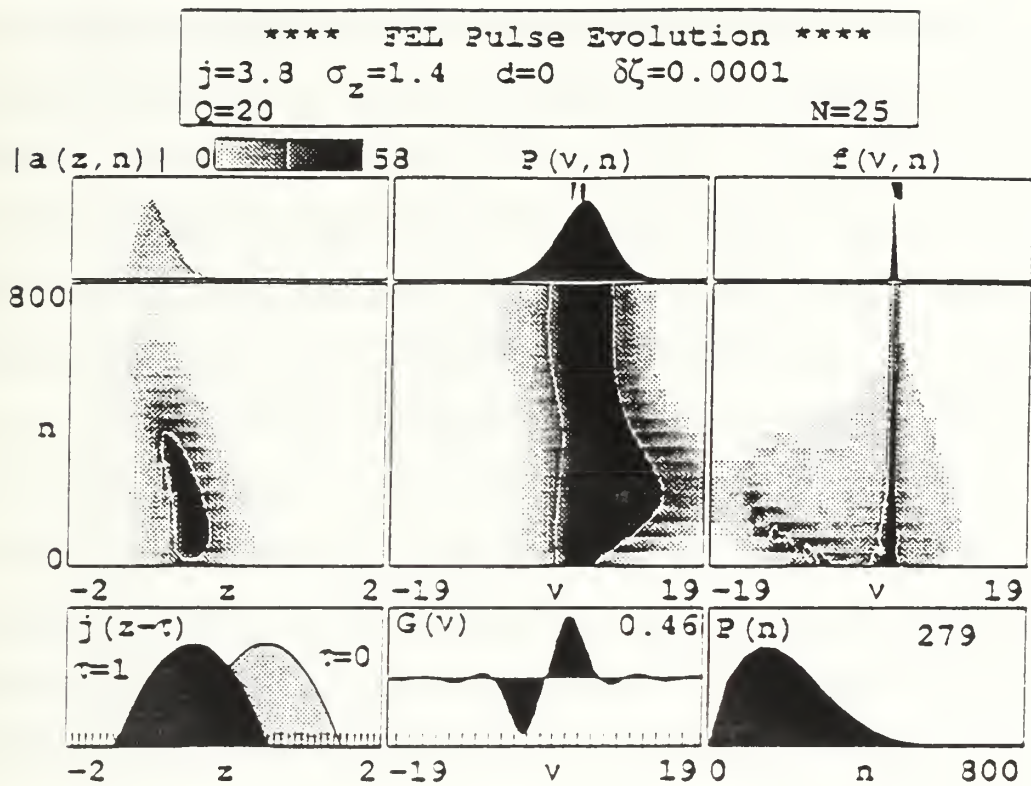


Figure 4-2: Short-pulse effects in an undulator with exact synchronism ( $d = 0$ ).

In order to start the optical pulse growth, random shot noise is generated by addition of a small phase,  $\delta\zeta = 0.0001$ , to each of the sample electron phases. The optical pulse is free to evolve subject to gain effects of the electron pulse, and resonator losses due to  $Q$  over  $n = 800$  passes through the undulator. Each pass, a new electron enters the undulator to drive the rebounding optical pulse. The shot noise creates a low power, broadband optical pulse in the first few passes with a length that is roughly equal to the sum of the slippage distance and the electron pulse length,  $\sigma_z + 1$ . This makes sense because this is the end-to-end distance over which the optical pulse is exposed to the amplifying electrons when at perfect synchronism.

The optical field is amplified at the rear of the optical pulse centroid after  $n \approx 10$  passes. The electrons are amplifying the optical pulse, which has partially passed over the electrons. It is clear that as the number of passes,  $n$ , increases, the centroid of the optical pulse moves backward (to the left) due to the continual amplification at the rear of the pulse. The amplitude evolution peaks near  $n \approx 200$  passes, and then decreases. The final shape of the pulse,  $|a(z,n)|$ , is shown, top-left, above the amplitude evolution plot. The maximum amplitude of the optical field is  $|a(z,n)| = 58$  is shown on the grey scale in black. A single contour line signifies half-maximum values, while zero amplitude is in white.

The power spectrum evolution (middle-center) starts near peak gain at  $v_0 \approx 2.6$ , and grows in width at  $n \approx 150$  passes. The broadened range of phase velocities  $v$  at this point is caused by a short pulse. The weak-field gain spectrum,  $G(v)$ , is plotted on the same scale below for reference. The final power spectrum,  $P(v,n)$ , shows the spread in phase velocities for the last pass,  $n = 800$ . The square tick-mark at the top of the power spectrum indicates the

center of the final power spectrum, while the pointed tick-mark shows the central wavelength of the initial radiation at resonance. The power evolution,  $P(n)$ , also shows rapid increase, peaking near  $n \approx 150$ , then tapers ultimately to zero power. The light wave in exact synchronism systems eventually drifts away from the slower electrons leaving the FEL with steady-state power of zero.

The electron beam phase velocity evolution (right-center) shows a single phase velocity emerging because of the vanishing optical power. On the final phase velocity plot,  $f(v,n)$  (right-top), the coincident initial and final phase velocity tick-marks indicate near-constant energy of the electron pulse due to a optical field.

In an undulator with desynchronism  $d > 0$ , the centroid of the optical pulse arrives at  $\tau=0$  slightly ahead of the centroid of the electron pulse which then passes back over the optical pulse. As the pulses propagate and  $\tau$  increases, the electrons bunch and radiate, amplifying the rear portions of the optical pulse with gain. The shape of the optical pulse is distorted with each successive pass through the undulator. Because the light pulse essentially grows from the rear, the light pulse will be distorted in amplitude over the slippage distance as the rear of the pulse grows. Figure 4-3 shows this effect with a small desynchronism  $d = 0.005$ , for the CEBAF IR FEL described in Fig 4-2.

In Fig 4-3, altering the FEL with small desynchronism  $d = 0.005$  results in major changes in performance of the laser system. The optical amplitude evolution survives and produces an amplitude in steady state at  $n \approx 300$  passes which has the dual-peak modulation in the final pass window  $|a(z,n)|$ .

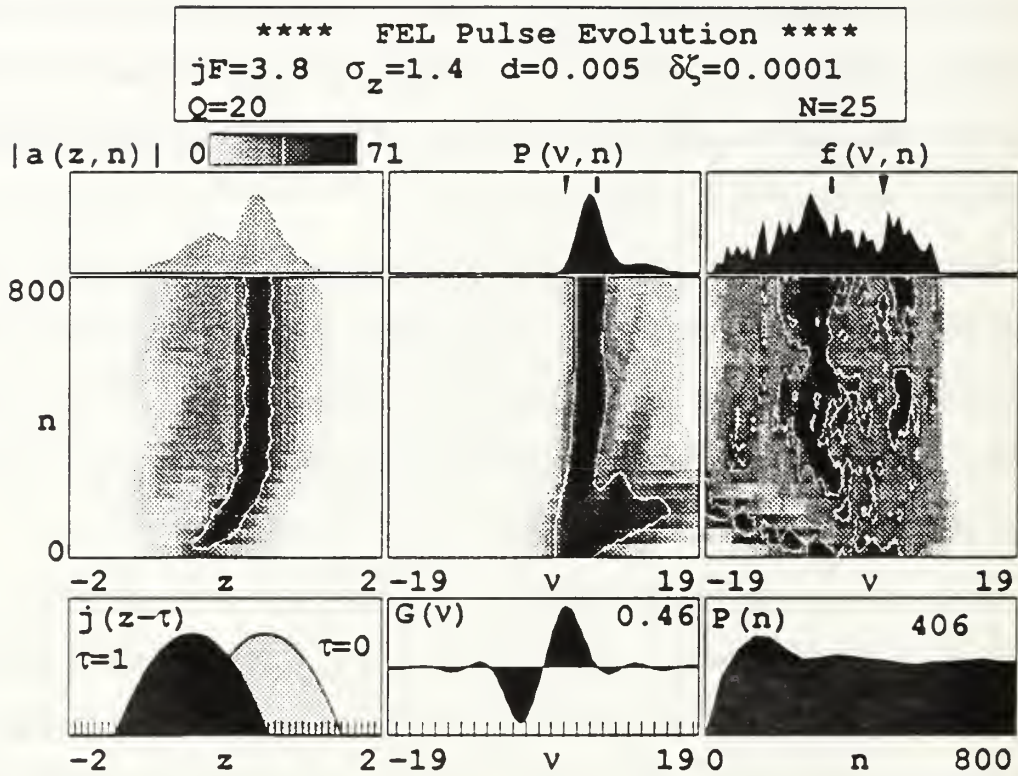


Figure 4-3: An FEL system with desynchronization and amplitude modulation due to short-pulse effects.

The power spectrum evolution,  $P(v,n)$ , and optical power,  $P(n)$ , also achieve steady state, with the maximum power much greater for this laser with non-zero desynchronism than the earlier synchronous FEL.

Though the final optical pulse shape  $|a(z,n)|$  is frozen in a single picture, the series of pictures for each successive pass shows the broad amplitude subpulses originate in an area of  $z \approx -1$ , and grow while moving to the right. This effectively describes the optical pulse being amplified along its rear, and a subpulse passing forward away from the slower electrons. The magnitudes of the subpulses would depend on the parameters of the system under simulation. The amplification and growth of the rear of the optical pulse also has the result that the centroid of the pulse moves at a speed less than  $c$ , which effectively lowers the pulse group velocity.

The tick marks in the final power spectrum picture shows the spread of center phase velocities expected, and there is a small sideband caused by trapped-particle instability. The wider spread of the electron spectrum  $f(v,n)$  is proportional to the separatrix peak-to-peak height, and the initial and final tick marks show a drop in electron phase velocities, indicating a net transfer of energy to the optical field.

The optical wavelength of an FEL is defined  $\lambda = \lambda_0((1 + K^2)/2\gamma^2)$ . In order to tune an FEL to a new wavelength, the undulator parameter,  $K = e\bar{B}\lambda_0/2\pi mc^2$ , is altered by changing the mean magnetic field  $\bar{B}$ . This in turn changes the optical mode waist,  $W_0$ , the filling factor,  $F$ , the dimensionless electron beam current,  $j$ , the dimensionless pulse length,  $\sigma_z = l_0/N\lambda$ , and several other FEL parameters. The effects short wavelengths for the CEBAF IR FEL operating at  $\lambda = 5\mu\text{m}$  is shown in Fig 4-4.



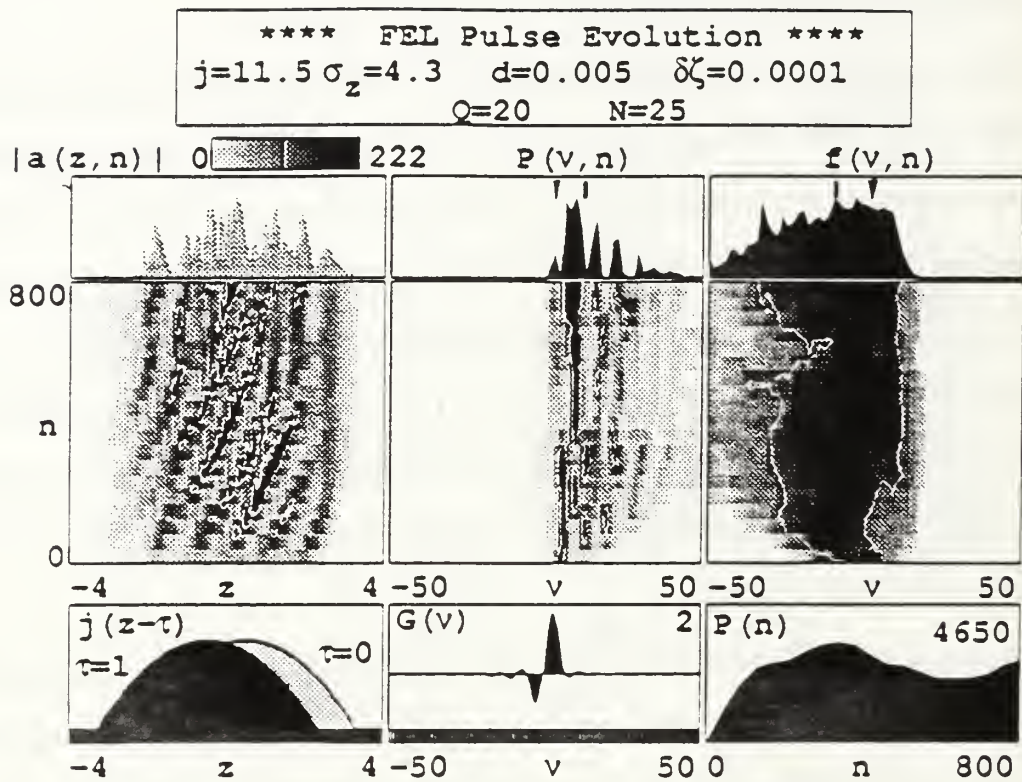


Figure 4-4: An FEL operating at  $\lambda = 5\mu\text{m}$  with long electron pulse length  $\sigma_z$ .

The dimensionless pulse length here is  $\sigma_z = 4.3$ , three times the length of the electron pulse for the FEL operating at  $\lambda = 15\mu\text{m}$  shown in Fig 4-3. The amplitude evolution plot clearly shows amplitude spikes growing from the rear of the optical pulse, and moving forward over several passes. The longer pulse results in a longer optical pulse spread along eight or ten slippage distances and  $|a(z,n)|$  amplitude spikes spaced roughly one slippage distance apart. In contrast to the narrow power spectrum of the short pulse FEL of Fig 4-3, here the power spectrum is spread among several sidebands without a steady-state.

Power evolution,  $P(n)$ , rises quickly but never achieves a steady value. The higher average power is a direct result of the longer electron pulse interacting with the optical pulse for a longer period and so transferring more energy. The electron spectrum,  $f(v,n)$ , of Fig 4-4 is again broad, with the average phase velocity dropping due to net energy transfer from the electrons to the optical pulse.

While electron pulse described by  $\sigma_z = 4.3$ , shown in Fig 4-4 has the smallest slippage within the tuning range  $5\mu\text{m} \leq \lambda \leq 20\mu\text{m}$ , the largest slippage is  $\sigma_z = 1.1$  at  $20\mu\text{m}$ . This system is shown in Fig 4-5. Figures 4-4 and 4-5 serve well to contrast the various effects of pulse length on system performance. Short-pulse effects generally result in short, narrow optical pulses spread over fewer slippage distances and comprised of fewer spikes.

Figure 4-6 shows an FEL operating near  $\lambda = 15\mu\text{m}$  with relatively high resonator losses,  $Q = 50$ , and a moderate desynchronism  $d = 0.0165$ . This higher value of  $d$  causes the modulation of the amplitude evolution to stand out clearly. [11]

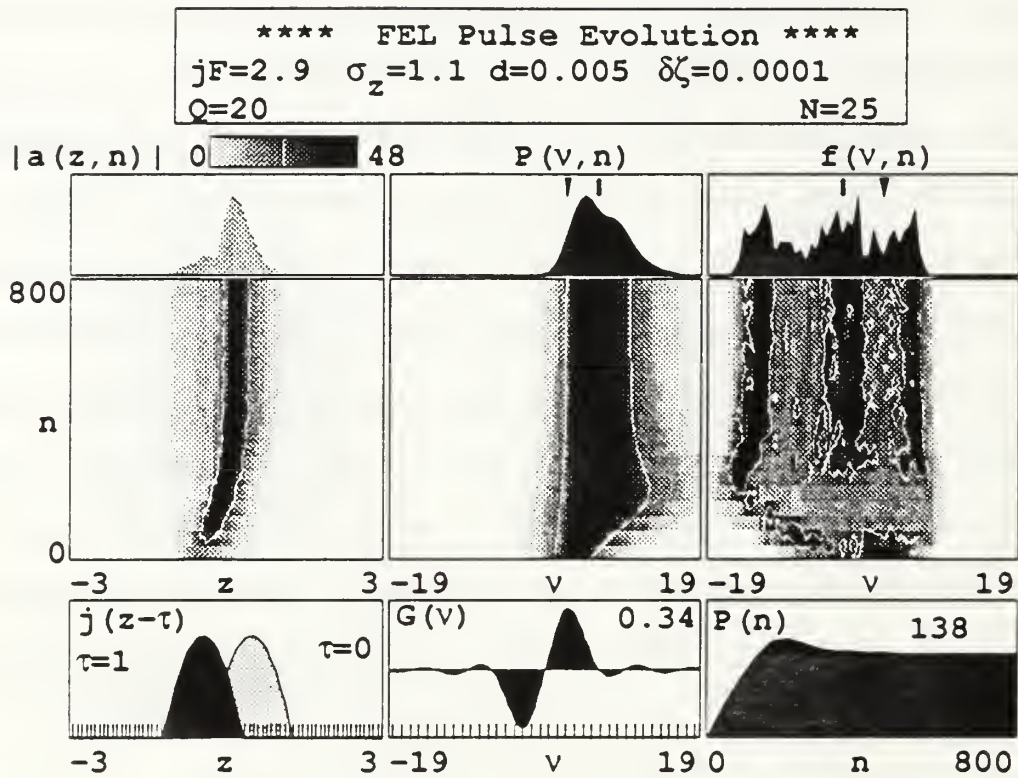


Figure 4-5: FEL operating at  $\lambda = 20\mu\text{m}$  and short electron pulse length  $\sigma_z = 1.1$ .

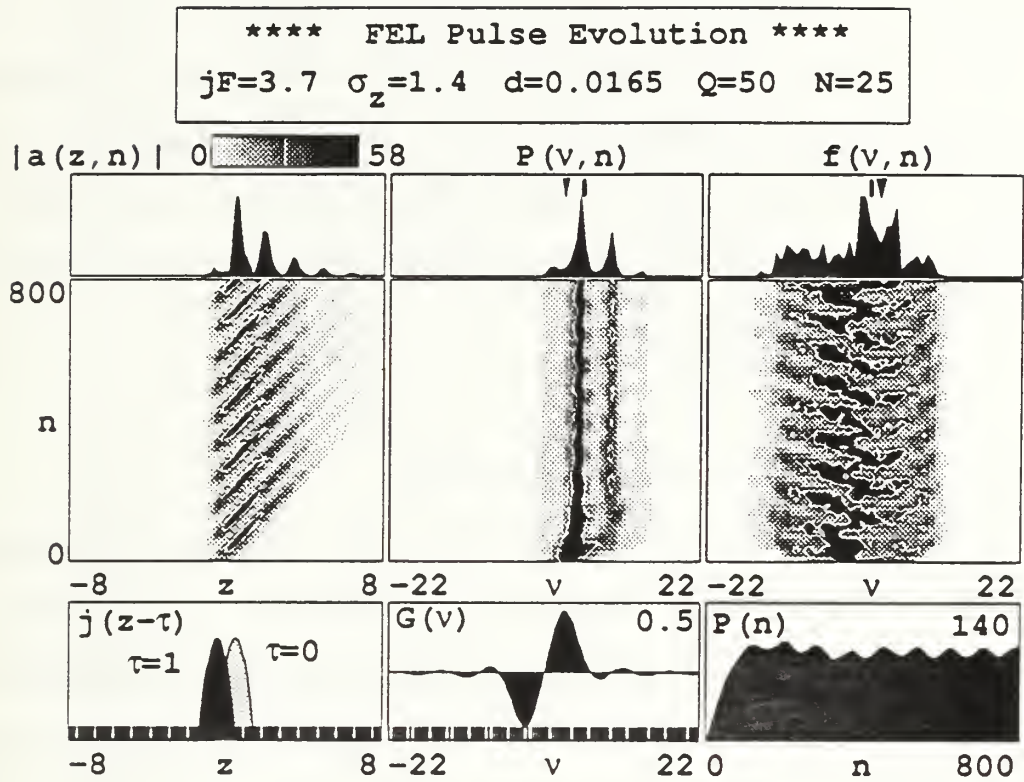


Figure 4-6: An FEL with steady state limit cycle behavior in the power evolution  $P(n)$ . [11]

The power evolution  $P(n)$  exhibits sharp overshoot followed by a steady state oscillation in power as new optical pulses grow periodically. The period of the oscillations appears to be  $\Delta n \approx 90$  passes. This oscillation is known as "limit-cycle behavior." This phenomena occurs in regimes of moderate desynchronism where a stable overlap does not occur between the optical pulse and the electron pulse. Moderate field strengths cause about one synchrotron oscillation, which causes the optical pulse to continually shift from one shape to another. [9,11]

#### D. CEBAF IR FEL TUNING RANGE AND GAIN

The tuning range of the CEBAF IR FEL ( $5\mu\text{m} \leq \lambda \leq 20\mu\text{m}$ ), combined with the effects of varying desynchronism on gain, allows for a broad range of system performance. The broad tuning range of the FEL includes electron pulse lengths ranging  $1.1 \leq \sigma_z \leq 4.3$ , which would imply a wide range of system gain. Neglecting the effects of the slight energy spread, and using multiple passes to achieve steady-state gain, simulations were run over a range of desynchronisms.

The shortest wavelength of the tuning range,  $\lambda = 5\mu\text{m}$ , has the longest pulse length  $\sigma_z = 4.3$ . Varying desynchronism  $d$  from 0.005 through 0.06 resulted in a steady single-pass gain of  $G = 170$  %. For wavelength  $\lambda = 10\mu\text{m}$ , with pulse length  $\sigma_z = 2.2$ , the gain is only about 60 %. At  $\lambda = 15\mu\text{m}$ , the gain is about 35 %. At the longest wavelength of this tuning range,  $\lambda = 20\mu\text{m}$ , the gain is about 20 %. Fig 4-7 shows the variation of the system gain across the wavelength tuning band of the CEBAF IR FEL.



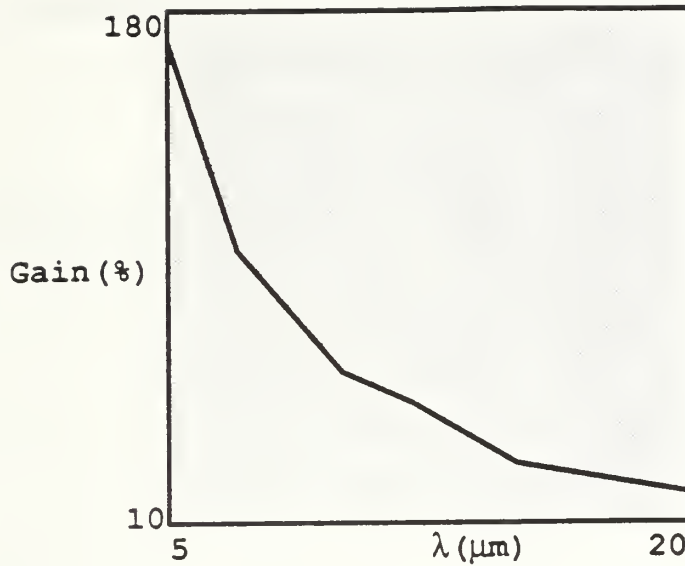


Figure 4-7: Gain as a function of wavelength  $\lambda$  for the CEBAF IRFEL.

The longest wavelength  $\lambda = 20\mu\text{m}$  has the lowest gain in the tuning bandwidth with  $G \approx 22\%$ . We considered lengthening the undulator from  $N = 25$  to  $N = 35$  periods in order to increase gain. The dimensionless current  $j$  increased from 138 to 379. The undulator length  $L$  increased from 150 cm to 210 cm, while the dimensionless electron pulse length decreased from  $\sigma_z \approx 1.1$  to 0.77. The average filling factor  $\bar{F}$  was reduced by half, but since  $j$  increased, the product  $j\bar{F}$  increased by a factor of three. While increasing  $j\bar{F}$  increases gain, the decrease in  $\sigma_z$  decreases gain. The net result from the lengthening of the undulator is determined by simulation. The gain is improved to  $G = 36\%$  for  $N = 35$  periods and  $G = 50\%$  for  $N = 45$  periods. The cost of increasing the

length of the undulator in order to improve gain at longer wavelengths would not be large.

## V. OPTICAL MODE DISTORTION

### A. BACKGROUND

After originating from spontaneous emission, the optical field in the undulator is a sum of rebounding light waves superimposed with newly generated light from the bunched electrons within the electron beam [15]. The longitudinal effects of short pulses were described in Chapter IV, and the transverse effects caused by natural diffraction and distortion by the electron beam will be treated in this chapter. The effects of short pulses will not be included in this chapter. For the CEBAF IR FEL  $F \approx 0.027$  [10]. As electron bunching develops late in the length of the undulator, the new light is created in an area that is  $\approx F$  times the size of the mode area. The newly created light from the small electron beam, has a short Rayleigh length and diffracts rapidly.

### B. GENERAL MODE DISTORTION

The effects of the small electron beam size acting on the optical mode may be simulated through numerical integration of the parabolic wave equation, 3-9, coupled with the Lorentz force equation, 3-1. To calculate the effects of mode distortion, it is necessary to shift the transverse dimensions into a dimensionless coordinate system, normalized to the mode size,  $x = x\sqrt{k/2L}$ . The optical amplitude,  $|a|$ , and the dimensionless current density,  $j$ , are also shifted into this coordinate system. The parabolic wave equation now becomes

$$\left[ -\frac{i}{4} \nabla^2 + \frac{\partial}{\partial \tau} \right] a(\mathbf{x}, \tau) = \langle j e^{i\zeta} \rangle, \quad 5-1$$

where the operator  $\nabla^2 = \partial^2/\partial x^2 + \partial^2/\partial y^2$ , properly describes the diffraction of the optical wave in transverse dimensions [13]. An important effect of diffraction is self-focusing of the optical mode back into the electron beam. The optical phase shift,  $\phi(\tau)$ , occurs in the center of the optical mode, near the electron beam, and acts to focus the light back onto the undulator axis. The FEL interaction causes the light to remain closer to the electron beam than would occur in the presence of natural diffraction alone. This effect is greater when gain is larger. When the optical mode is larger than  $\sqrt{2L/k}$  the distortion operator  $\approx 1$ , and can be neglected. [13]

### C. MODE DISTORTION SIMULATIONS

Figure 5-1 shows a numerical simulation of a Gaussian optical wavefront propagating without the effects of electron beam current ( $j = 0$ ), as  $\tau$  goes from 0 to 1 in an undulator with  $N = 25$  periods. The wavefront has weak initial optical field amplitude,  $a_0 = 1.0$ , at mode center, and mode curvature giving normalized Rayleigh length of  $z_0 = 0.5$  focussed at  $\tau_w = 0.5$ . Transverse dimensions are normalized to the mode waist  $\sqrt{k/2L}$ . The grey scale at upper right shows the intensity for minimum (white), and for maximum (black), with five white contour lines to illustrate the focusing and diffraction of the light wave.

The optical amplitude evolution plot,  $|a(x, \tau)|$ , (upper-left) shows the optical mode evolution over a single pass through the undulator. The five contour lines show the focusing and diffraction expected for an undistorted optical wavefront. The optical amplitude is greatest at the mode center, and decreases radially as shown in the transverse optical amplitude plot,  $|a(x, y)|$ , representing the final mode at the end of undulator. The optical phase shift,  $\phi(0, \tau)$ , shifts negatively,  $\Delta\phi \approx -\tau/z_0$ , during diffraction.

Figure 5-2 shows an FEL with the same optical parameters as shown in Fig 5-1, but with optical mode distortion caused by an electron beam current  $j = 138$  for the CEBAF IR FEL. The electron beam has normalized radius,  $\sigma_x \approx r_b / \sqrt{L\lambda\pi} = 0.125$ , and has initial phase velocity  $v_0 = 4.6$ . With a single contour line, the optical amplitude plot,  $|a(x,\tau)|$ , shows focusing of the light with Rayleigh length  $z_0 = 0.5$  in toward the mode waist positioned at  $\tau_w = 0.5$ . Relative to the undistorted field of Fig 5-1, the field distortion in Fig 5-2 is clear. The maximum amplitude,  $|a(x,\tau)|$ , is greater, and the contour line spreads rapidly from the beginning of the undulator as the distortion of the electron beam drives up the amplitude of the optical mode along the second half of the undulator. The final transverse amplitude plot,  $|a(x,y)|$ , shows the relatively narrow mode focussed around the electron beam. The electron bunching current,  $\sigma(x,\tau) \propto j(r)\langle\cos(\zeta,\phi)\rangle$ , evolves as the electron phases,  $\zeta$ , bunch within each optical wavelength. The plot of final electron bunching,  $\sigma(x,y)$ , shows the relative disparity in size of the electron beam relative to the final optical mode,  $|a(x,y)|$ . [11]

The electron phase velocity evolution,  $f(v,\tau)$  in Fig 5-2, starts at  $v_0 = 4.6$ , and broadens slightly due to bunching. There is also slight bunching shown in the phase-space plot,  $(\zeta,v)$ . The optical phase shift,  $\phi(0,\tau)$ , is also affected by distortion effects of the beam current,  $j$ . From 5-1, the FEL optical phase shift  $\phi = j\langle\sin(\zeta + \phi)\rangle/|a|$ , is maximized at  $(\zeta + \phi) = \pi/2$ . The electron phase,  $\zeta$ , is a function of dimensionless time,  $\tau$ , so that for strong-field FEL interaction,  $\phi \approx j\tau/|a|$ , and for weak fields,  $\phi \approx j\tau^3/12$ . [9]



# FEL WAVEFRONTS

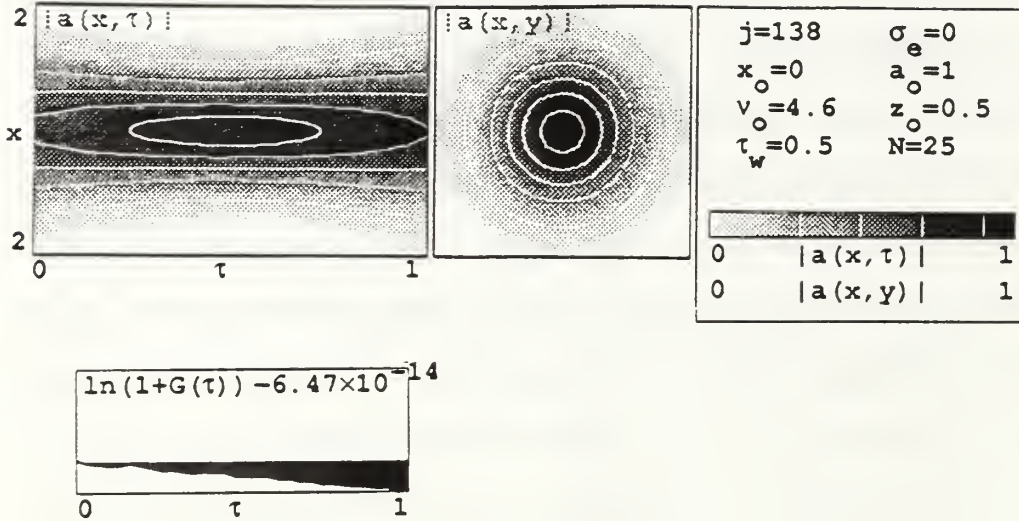


Figure 5-1: Non-distorted optical mode propagation diffraction.

In either a strong or weak fields, the FEL interaction gives a positive shift to the optical phase. Variation of  $\phi(0, \tau)$  as  $\tau$  increases from 0 to 1 is driven by electron beam interaction.

Exponential growth of gain and power is delayed in the undulator until the bunching time,  $\tau_B \approx (2/j)^{1/3} \approx 0.25$ , has passed, after which the strong beam current,  $j$ , drives up the gain and power [9]. The gain for the FEL in Fig 5-2 is  $\ln(1 + G(\tau)) = 0.846$  or  $G \approx 133\%$ . Theoretical single-mode gain for this system predicts only  $G_0 \approx 0.135 j F \approx 43\%$ . In single-mode theory, the dimensionless current density,  $j$ , is proportional to the electron beam density,  $\rho$ , and is therefore inversely proportional to the square of the electron beam radius, or  $j \propto r_e^{-2}$ . [11]

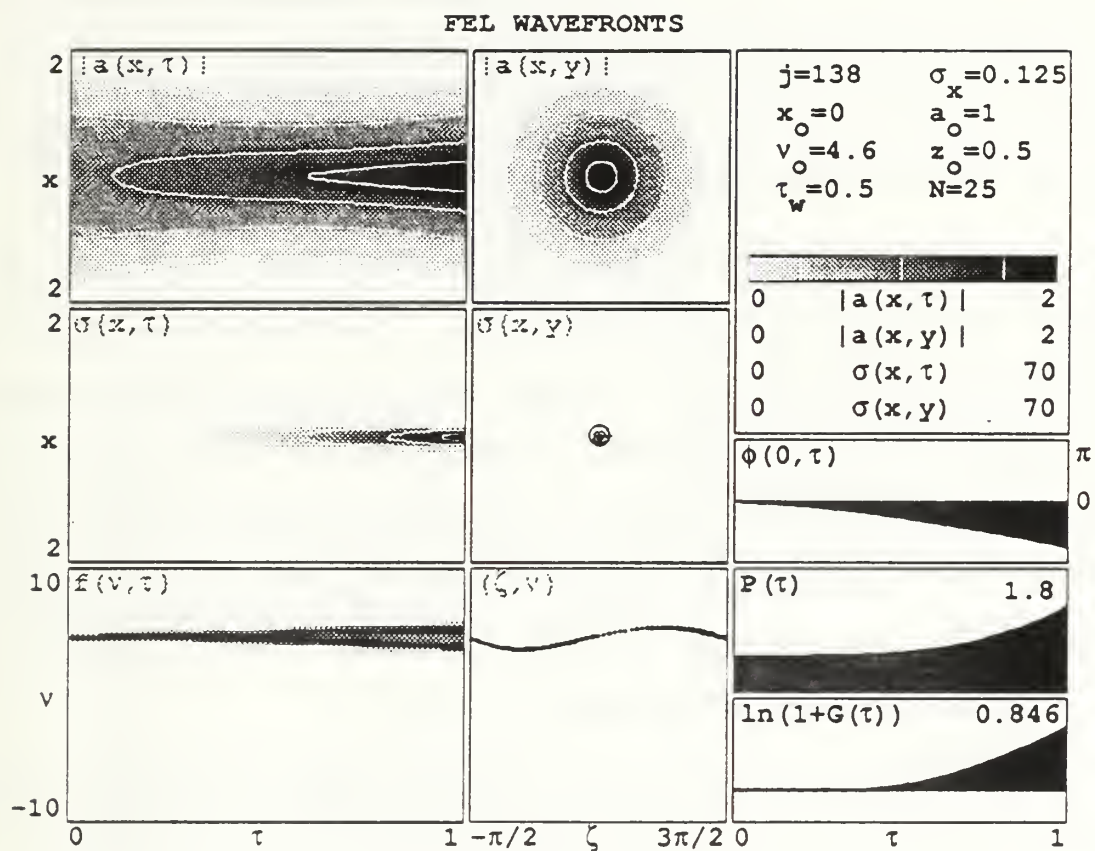


Figure 5-2: FEL with optical mode distortion. [11]

The filling factor,  $F$ , is proportional to the electron beam radius,  $F \propto r_e^2$ , and so the theoretical gain,  $G_0 \propto jF$ , becomes independent of the electron beam size as long as the electron beam is contained within the optical mode. But single-mode theory does not account for the mode distortion caused by the intense current and small filling factor of the FEL in Fig 5-2. [11]

Figure 5-3 shows the effects of shifting mode waist position,  $\tau_w$ , and Rayleigh length,  $z_0$ , to achieve increased gain. Showing strong diffraction and distortion effects, the amplitude evolution,  $|a(x,\tau)|$ , shows the light focussed inward to  $\tau_w = 0.19$ , and then sharply diffracting outward from a narrow waist near  $\tau \approx 0.40$ . This is due in part to the short Rayleigh length,  $z_0 = 0.14$ , which causes light to diffract rapidly. The plot of the final mode,  $|a(x,y)|$ , clearly shows the narrow focusing of the optical mode around the electron beam, and the rapid spread of highly diffracted light.

The larger, irregular shift of  $\phi(0,\tau)$  for the FEL in Fig 5-3 is due to the short Rayleigh length,  $z_0 = 0.14$ , and the varying effects of the field amplitude  $|a|$  along the undulator. The apparent discontinuity late in the plot of  $\phi(0,\tau)$  represents the optical phase shift decreasing to  $\approx -\pi$ . Electron bunching occurs later in the undulator than for the FEL of Fig 5-2, as shown by the bunching current plot,  $\sigma(x,\tau)$ . The final gain is much greater than for Fig 5-2, with  $\ln(1 + G(\tau)) = 1.14$ , or  $G(\tau) \approx 212\%$ . Single-mode theory, neglecting the effects of mode distortion, predicts this FEL to have gain  $G_0 \approx 40 \%$ .

# FEL WAVEFRONTS

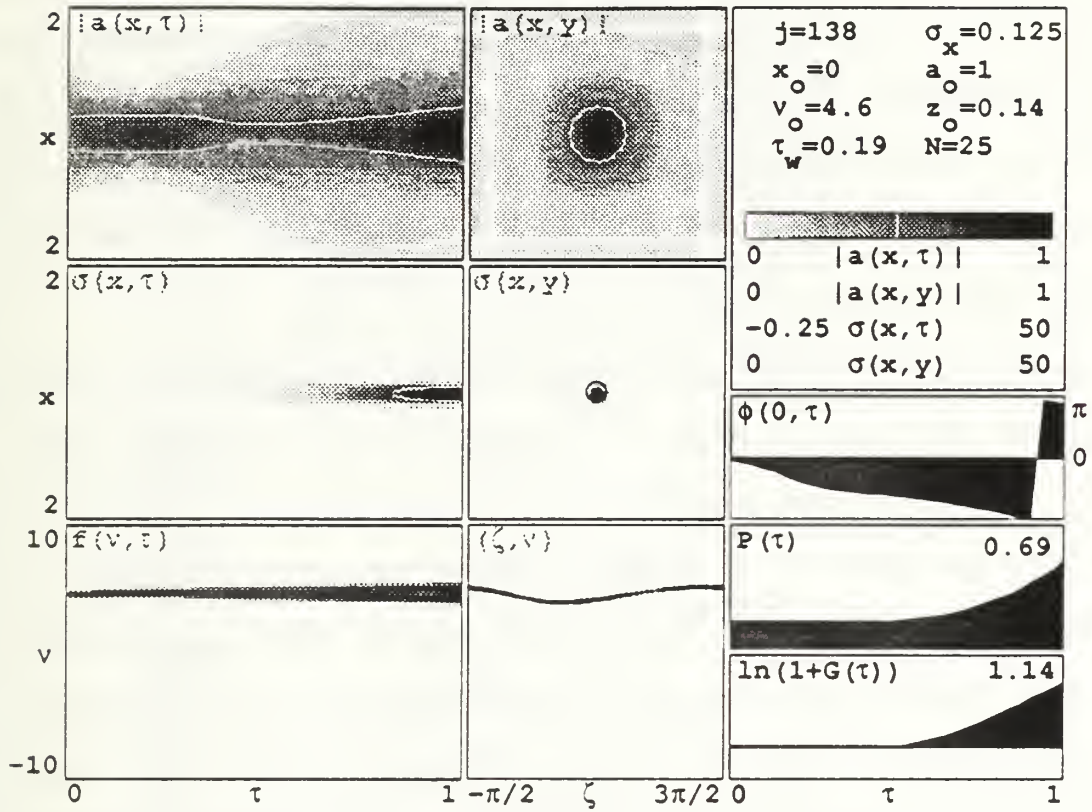


Figure 5-3: An FEL with short Rayleigh length and high distortion.

## D. MODE PARAMETERS, RESONANCE AND GAIN

Variation of Rayleigh length and mode waist position and the resultant gain curves are shown in Figures 5-4 and 5-5. Typical values for Rayleigh length and mode waist position are  $z_0 = \pi W_0^2 / L\lambda = Z_0 / L \approx 1/\sqrt{12}$  or  $z_0 \approx 0.5$ , and  $\tau_w \approx 0.5$ , but simulations for the CEBAF IR FEL produced peak gain at  $z_0 \approx 0.33$ . Using this Rayleigh length, the peak gain for variation of mode waist position was located at  $\tau_w \approx 0.35$ .

Figure 5-6 shows the optical gain spectrum,  $G(v_0)$ , plotting the gain against the FEL phase velocity,  $v_0 = L[(k+k_0)\beta_z - k]$  [7]. Rayleigh length,  $z_0 = 0.14$ , and mode waist position,  $\tau_w = 0.19$ , are selected to maximize the single-pass gain for the small CEBAF electron beam. When  $\lambda \approx 15 \mu\text{m}$ , the CEBAF IR FEL is near resonance  $v_0 \approx 0$ , and Fig 5-6 shows the gain around resonance. When the phase velocity is off-resonance by  $\Delta v_0 = \pi$ , the shift in wavelength is  $\Delta\lambda/\lambda \approx \Delta v_0 / 2\pi N \approx 1/2N \approx 2\%$ . The electron beam has a radial parabolic shape described by  $j(r) = j(1 - r^2/2\sigma_\theta^2)$  for  $r < \sqrt{2}\sigma_\theta$ , and zero otherwise. The peak current is  $j = 138$ , and the normalized beam radius is  $\sigma_\theta = r_\theta \sqrt{\pi/L\lambda} \approx 0.125$ . [11]

The simulation in Fig 5-6 calculates gain including the transverse effects of diffraction, but ignores the longitudinal short-pulse effects. At each value of  $v_0$ , a wavefront enters the FEL undulator with peak field strength  $a_0 = 1$  in the weak field regime, where  $a_0 = 4\pi NeKLE/\gamma^2 mc^2$ , and  $E$  is the optical electric field strength. The peak gain in Fig 5-6 is  $G \approx 233\%$  at phase velocity  $v_0 \approx 5$ . The region of positive gain is larger than the region of negative gain, as is typical of high current FELs [9]. The gain spectrum tails off smoothly as  $v_0$  increases on the right of Fig 5-6. [11]



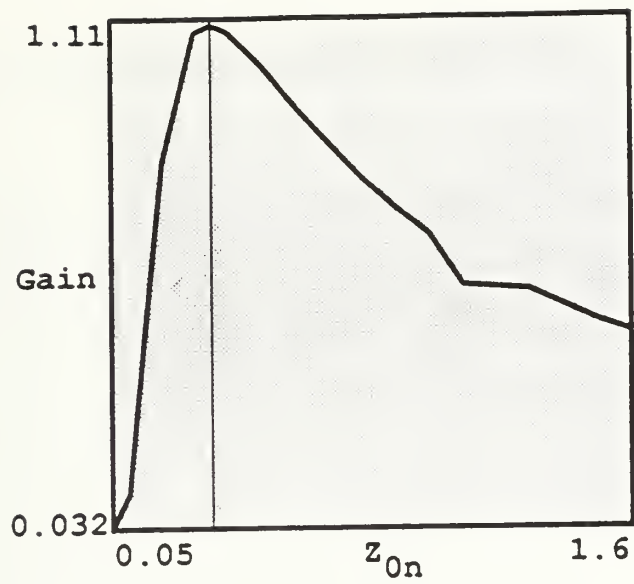


Figure 5-4: Variation of gain with Rayleigh length,  $z_0$ .

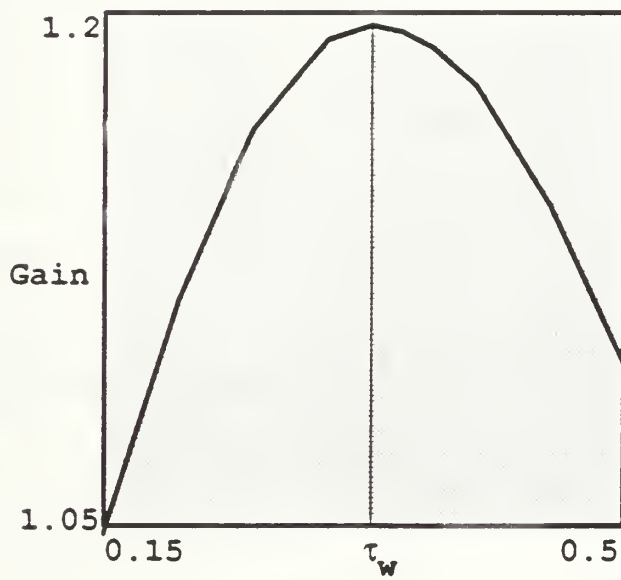


Figure 5-5: Variation of gain with mode waist position,  $\tau_w$ .

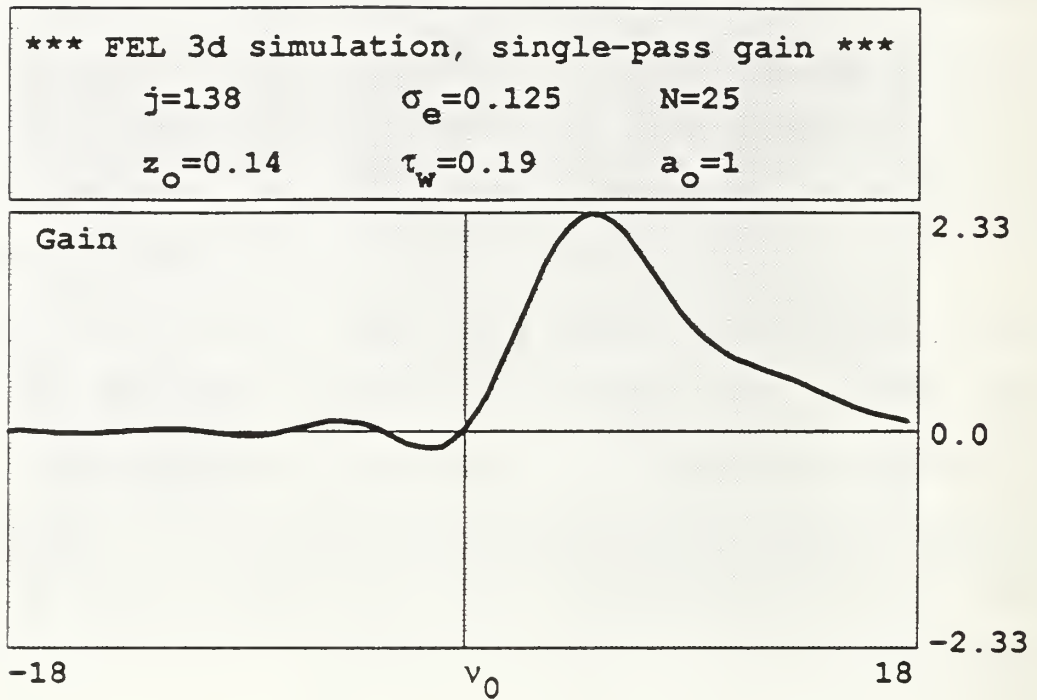


Figure 5-6: The optimized CEBAF IF FEL gain spectrum including only transverse modes.

## E. GAIN AND SMALL ELECTRON BEAMS

The FEL gain observed for Figs 5-2 and 5-3 indicates that single-mode theory can significantly underestimate the effects of diffraction and distortion on actual FEL gain. Calculating the single-pass gain over a broad range of filling factors, the dependence of FEL gain on electron beam size is examined in Fig 5-7. Neglecting optical mode distortion, the single-mode FEL gain is  $G_0 \approx 0.135j\bar{F}$ . The gain ratio  $G/G_0$  is determined numerically and plotted as a function of the electron beam size compared to the optical mode waist,  $\sigma_e/w_0$ , with a single line on the plot signifying  $G/G_0 = 1.0$ . The product of the peak beam current and the beam area,  $j\sigma_e^2 \propto j\bar{F}$ , is held constant at  $j\bar{F} = 0.1$ . The electron beam shape is taken to be parabolic,  $j(r) = j(1-r^2/2\sigma_e^2)$  for  $r < \sqrt{2}\sigma_e$  and zero otherwise. A small value of  $j\bar{F}$  is used to insure that there are no high gain effects for values on the left side of Fig 5-7 where  $\bar{F} = \sigma_e^2/w_0^2$  is small and  $j$  may be large. The Rayleigh length is,  $z_0 = 1/\sqrt{12} \approx 0.29$ , for optical single-mode gain  $G_0$  and position of the mode waist is,  $\tau_w = 0.5$ . These values are chosen to describe a more typical FEL mode instead of the optimized CEBAF IR FEL. The phase velocity is  $v_0 = 5$  for peak single-mode gain [12], and the peak optical amplitude is  $a_0 = 1$  for weak fields. [11]

The plot shows a clear dependence on the electron beam size at all values plotted. The single-mode theory is correct for the range of values  $\sigma_e/w_0$  where the  $G \approx G_0$ . We see that there is no range of values where the single-mode theory is correct, but only a single point. For a small electron beam, the single-pass gain including many modes can be significantly higher than the single-mode gain,  $G_0$ . It is emphasized that the mode distortion crucial to the increased value of  $G/G_0$  is not caused by high current. [11]

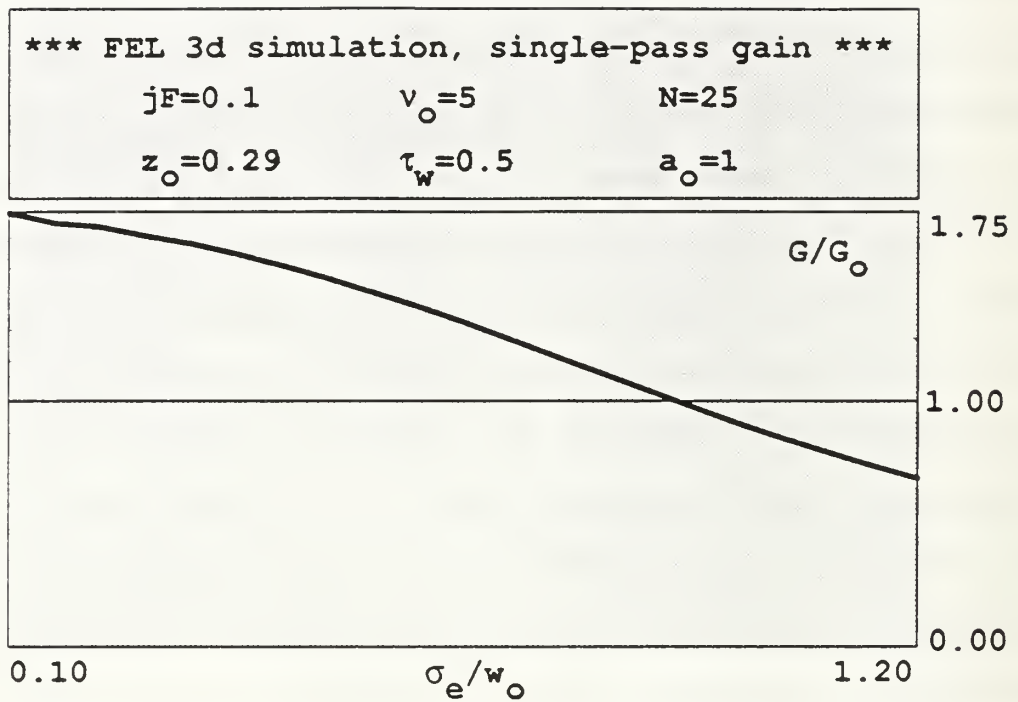


Figure 5-7: General gain curve for FELs with small electron beams.  
[11]

When the product  $j\bar{F}$  is decreased by  $\times 100$  to  $j\bar{F} = 0.001$ , the plot in Fig 5-7 remains substantially the same. When  $j\bar{F}$  is increased to unity, or above, the gain enhancement due to mode distortion is further increased by high-gain effects on the left side of Fig 5-7 where beam radius is small and  $j$  is large. It is not clear from this analysis what part of the distorted mode will remain in a resonator after many passes. The actual gain of an FEL oscillator may be reduced from that shown in Fig 5-7 depending on the resonator design [13,15,16]. No known work explains Fig 5-7, and in particular, its independence of the value of  $j\bar{F}$  below unity, where there is vanishingly small mode distortion. [11]

## F. PROPAGATION AND INTERFERENCE

A modification of the simulation that produced Figures 5-1 to 5-3 subtracts the input optical field from the total field to allow analysis of the propagation of newly created light during a single pass through the undulator. This process is interesting because of the complex optical field interactions shown in Fig 5-8. Because the amplitude plots,  $\Delta|a(x,\tau)|$  and  $\Delta|a(x,y)|$ , are generated by subtraction, it is possible to have negative amplitude values, representing destructive interference in the total optical field, reducing field amplitude. Destructive interference occurs when "new" light from the bunching of electrons encounters "old" light with phase difference of  $|\Delta\phi| = \Delta\tau/z_0 = \pi$  radians. Noting that the newly generated light appears in the amplitude evolution,  $\Delta|a(x,\tau)|$ , near  $\Delta\tau \approx 1/3$ , and holding optical mode waist,  $w_0 \approx [z_0 + 1/12z_0]^{1/2}$ , constant by the input Rayleigh length,  $z_0 \approx w_0^2 \approx \sigma_\theta^2$ , a phase shift relationship may be found:



# OPTICAL MODE DISTORTION: PROPAGATED

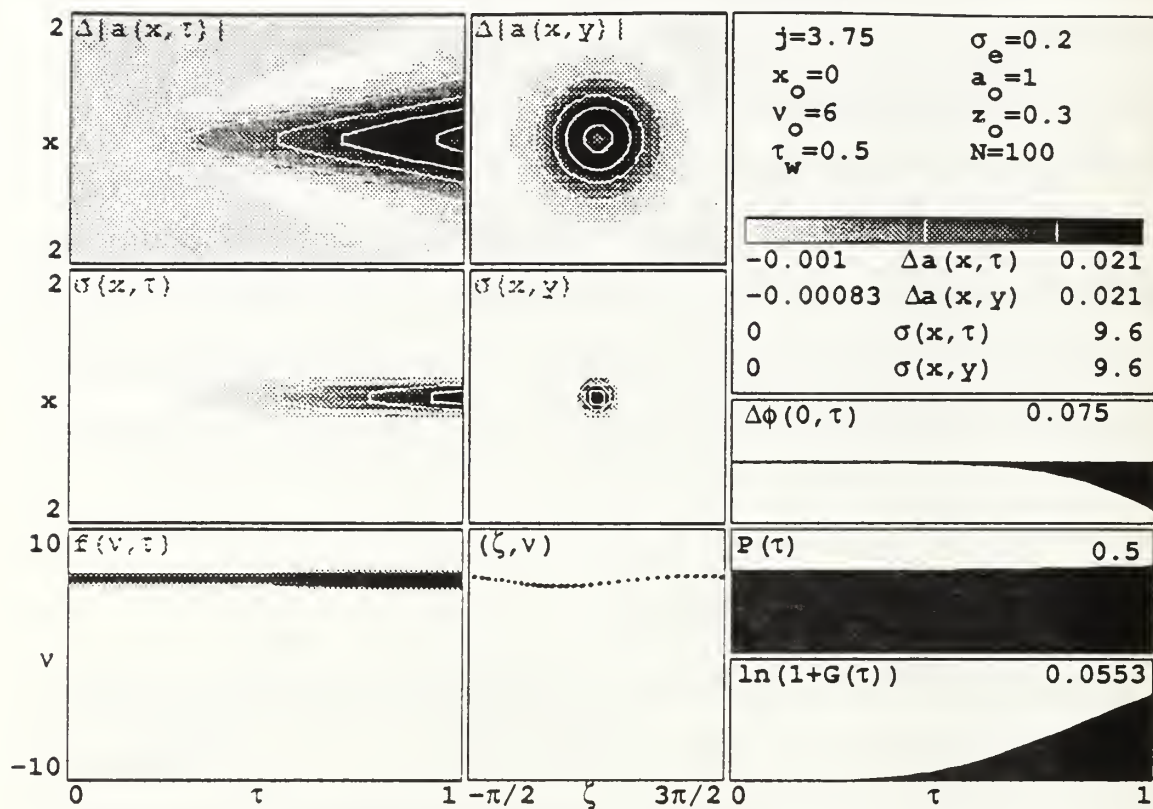


Figure 5-8: Negative interference of propagated light.

$$\Delta\phi \approx \frac{\Delta\tau}{z_0} \approx \frac{\Delta\tau}{\sigma_\theta^2}, \quad \sigma_\theta \approx \sqrt{\frac{\Delta\tau}{\Delta\phi}} \approx \sqrt{\frac{1}{3} \frac{1}{\pi}} \approx 0.3. \quad 5-2$$

For electron beam radius,  $\sigma_\theta \leq 0.3$ , conditions for destructive interference may exist.

The plot of propagated optical amplitude evolution,  $\Delta|a(x,\tau)|$ , shows an area of destructive interference starting near  $\tau \approx 0.7$ , which is obvious in the final amplitude plot,  $\Delta|a(x,y)|$ , as a light area in the center of the optical mode. To evaluate the interference effect over a range of values of  $j\sigma_\theta^2$ , the product was held constant while  $j$  and  $\sigma_\theta$  were varied. Destructive interference was observed for  $0.12 \leq \sigma_\theta \leq 0.3$ , and the point of initial destructive interference occurred earlier in the undulator as the electron beam,  $\sigma_\theta$ , is narrowed. This is in part caused by the constant product  $j\sigma_\theta^2$ , which rapidly raises beam current,  $j$ , as the electron beam narrows. This appears as a radial 'dimple' across the propagated wavefront after a single pass through the undulator. In order to determine whether the phenomenon of destructive interference in the optical wavefront continues outside the undulator, a multi-pass simulation within the entire resonator is required. This destructive interference over a single pass was first investigated by LT Carl Bice in his thesis in December, 1991, and is a continuation of that work.[14]

## VI. MULTI-PASS OPTICAL MODE DISTORTION

### A. BACKGROUND

To continue the investigation of mode distortion, the single-pass three dimensional simulation used in Chapter V is modified to calculate the transverse beam effects over multiple passes. This enables further research into the interference effects shown in Fig 5-8, and the relationship between gain and electron beam size as shown in Fig 5-7. The multiple pass simulations introduce optical mode selection caused by the finite size of the resonator mirrors. Through many passes, highly diffracted modes may be lost due to mirror size and placement.

### B. MULTIPLE PASS PROPAGATION AND INTERFERENCE

Investigation of the single-pass optical interference pattern shown in Fig 5-8 over multiple passes will be affected by the number of passes,  $n$ , and the mirror design. Figure 6-1 shows the three dimensional simulation modified for multiple passes. For this regime, the initial optical amplitude,  $a_0 = 0.05$ , for a weak field system. At either end of the amplitude plot,  $|a(x,n)|$ , are curved mirrors, spaced  $\tau_m = 2$  apart, or twice the undulator length. The separation distance of a typical FEL may be larger, but this choice allows ease of computation. The dimensionless mirror radius of curvature,  $r_c$ , is determined by the mirror spacing,  $\tau_m$ , and the normalized Rayleigh length:  $r_c = \tau_m/2 + 2z_0^2/\tau_m$ . The actual mirror radius of curvature is given by  $Lr_c$ . The mirror losses are described by  $Q = 50$ , and the mirror edge-loss is  $\kappa = 0.001$ .

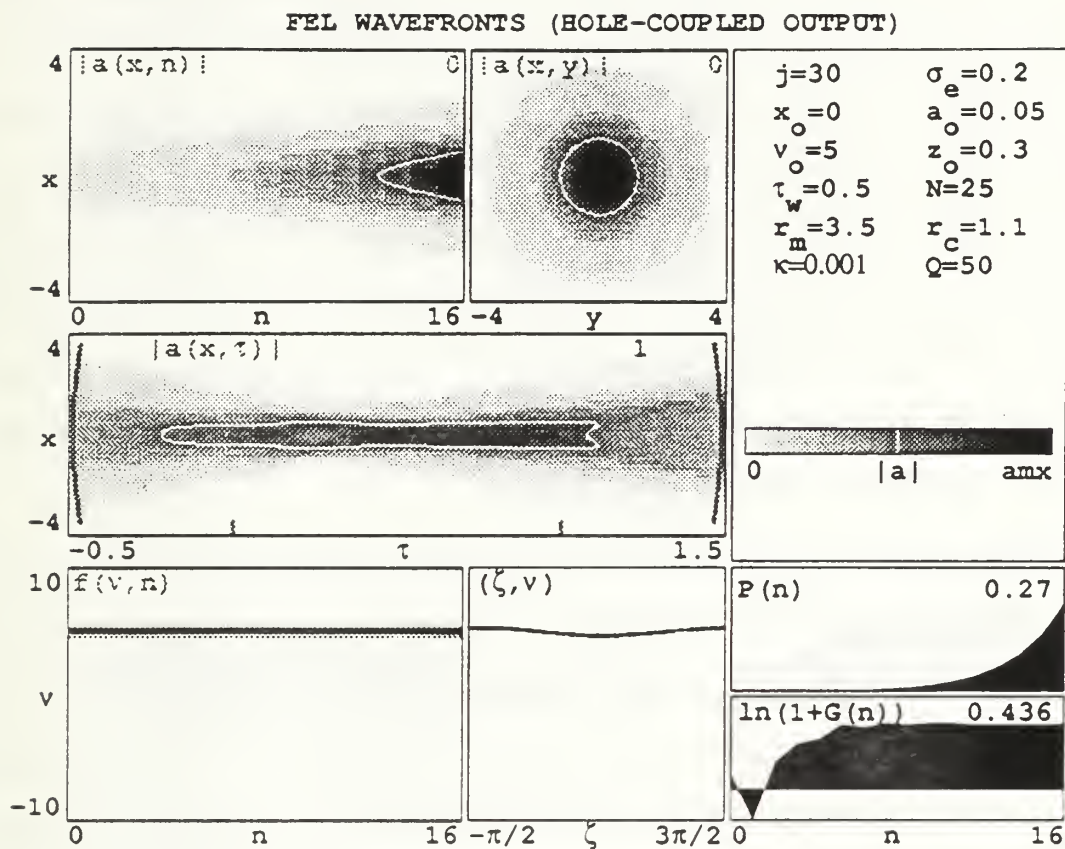


Figure 6-1: Three dimensional simulation for multiple passes and destructive interference.

Edge-losses occur when the mirror radius,  $r_m$ , is not wide enough to capture the higher-order optical modes, losing them to the non-reflecting sides of the resonator. The dimensionless mirror radius is a function of the Rayleigh length, mirror spacing and edge loss,  $r_m = [z_0 (1 + \tau_m^2/4z_0^2) (1/2 \log((1 + \kappa)/\kappa))]^{1/2}$ . The amplitude plot,  $|a(x,n)|$  (upper-left), shows the evolution and growth of the optical mode through  $n = 16$  passes, as scaled along the base of the plot. The single contour line shows that the amplitude begins to grow in the last few passes. The plot of resonator mode evolution,  $|a(x,\tau)|$  (center), shows the entire optical mode at pass  $n = 16$ . The undulator ends are represented by tick marks at  $\tau = 0$  and  $\tau = 1$  along the plot base.

Careful analysis reveals that a radial "dimple", similar to that found in the single-pass interference plot of Fig 5-8, is present near the right end of the optical mode. In the grey scale used, the destructive interference described in Chapter V is present as two unshaded rays that propagate from just outside the undulator markings toward the right-side mirror. The final transverse amplitude plot,  $|a(x,y)|$ , shows the amplitude at the last pass,  $n = 16$  at the end of the undulator.

The electron phase velocity evolution,  $f(v,n)$ , shows only small modulation in weak fields. The phase-space plot,  $(\zeta,v)$ , shows slight bunching in this weak field regime. Power evolution,  $P(n)$ , starts to grow at approximately the same point as the amplitude in  $|a(x,n)|$ . Gain,  $G$ , reaches a steady-state near  $n = 8$ , where  $G \approx 55\%$ , and single-mode gain  $\cdot G_0 \propto j\mathcal{F}$  predicts only 28%.

Figure 6-2 shows an FEL similar to that of Fig 6-1, but in the strong field regime, starting with  $a_0 = 5.0$ , and running over  $n = 160$  passes. The amplitude evolution plot,  $|a(x,n)|$ , has a much greater maximum of 39.



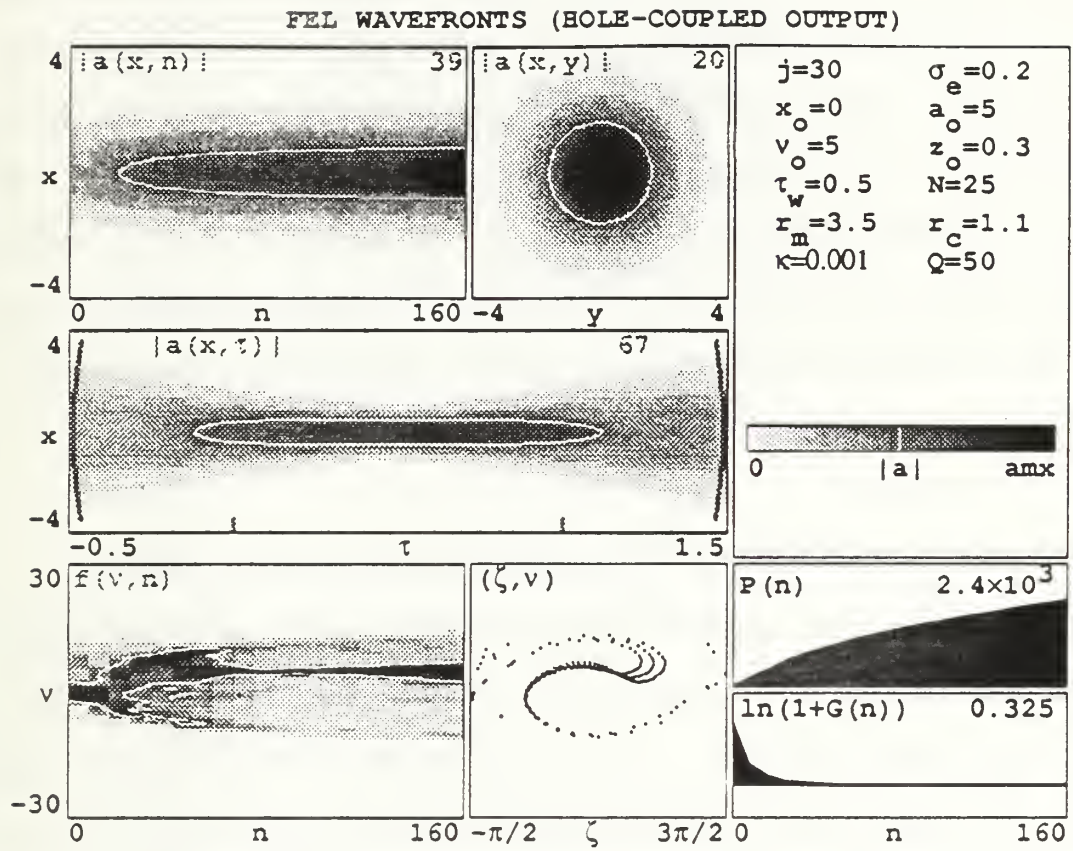


Figure 6-2: Three dimensional simulation without destructive interference.

The final transverse amplitude plot,  $|a(x,y)|$ , and the resonator plot,  $|a(x,\tau)|$ , show an optical mode with no radial "dimple". The phase evolution plot,  $f(v,n)$ , and phase-space plot,  $(\zeta,v)$ , show complex bunching due to strong field saturation. Power evolution,  $P(n)$ , starts near where the amplitude plot begins to grow, and continues to increase through the  $n = 160$  passes. If this simulation continued for more passes, the power evolution,  $P(n)$ , would achieve a steady state value. The gain plot shows an early peak, followed by a quick reduction to near-zero steady-state near  $n \approx 50$ . It appears that the interference "dimple" is not present at saturation in the FEL oscillator.

### C. GAIN AND SMALL ELECTRON BEAMS OVER MULTIPLE PASSES

To investigate the effects of electron beam size on gain over multiple passes, the product  $j\sigma_e^2$  is held constant, while the electron beam radius is decreased. Actual FEL gain,  $G$ , was numerically calculated over several passes, while the single-mode gain is given by  $G_0 \approx 0.135j\mathcal{F} \propto j\sigma_e^2$ . In order to determine whether the single-pass relationship of gain on electron beam size shown in Fig 5-7 applies for multiple passes through the resonator, simulations were run to evaluate gain. For these simulations, mirror loss are  $Q = 1000$ , and the edge loss is  $\kappa = 0.001$ . The Rayleigh length,  $z_0$ , edge loss,  $\kappa$ , and mirror spacing,  $\tau_m$ , result in mirror radius,  $r_m = 2.7$ , and radius of curvature  $r_c = 0.9$ .

Figure 6-3 shows the ratio of the actual gain to the single-mode gain,  $G/G_0$ , plotted against the ratio of dimensionless beam radius to mode waist,  $\sigma_e/w_0$  while holding  $j\sigma_e^2 = 0.4$ . Fig 6-4 shows a similar plot for the value  $j\sigma_e^2 = 0.6$ . To prevent the influence of high-gain effects, the beam radius is limited by  $\sigma_e/w_0 > 0.1$ .

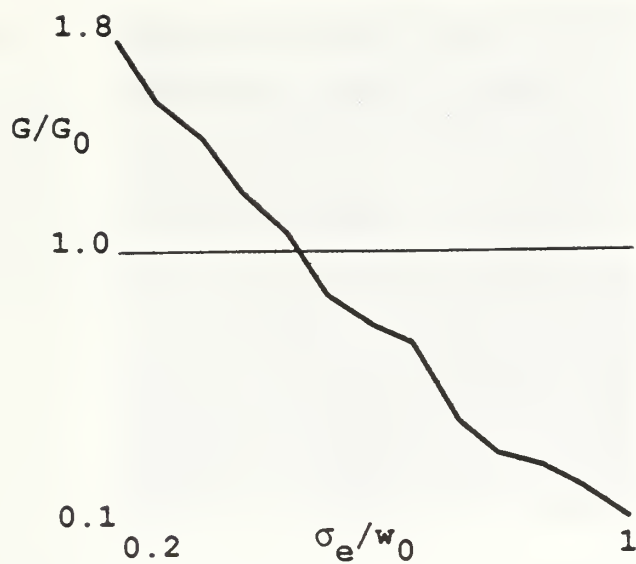


Figure 6-3: Multiple-pass gain curve for  $j\sigma_\theta^2 = 0.4$ .

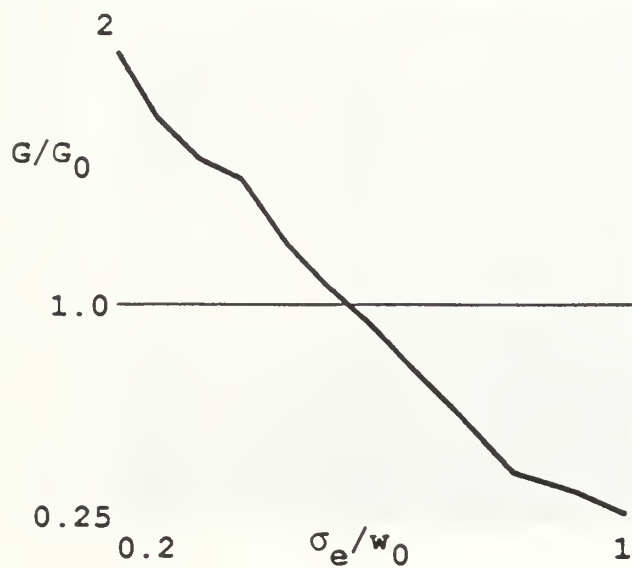


Figure 6-4: Multiple-pass gain curve for  $j\sigma_\theta^2 = 0.6$ .

The curves resemble the single-pass results in Fig 5-7, with the gain ratios decreasing steadily as the electron beam radii widen toward the size of the mode waist. The single-mode gain product  $j\sigma_{\theta}^2$  is greater for Fig 6-4, so the gain curve for Fig 6-4 is higher than for Fig 6-3. Similar to Fig 5-7, there is no range of values where single-mode theory is correct, only single points where  $G/G_0 \approx 1$ .

## VII. CONCLUSIONS

The development of the FEL as a useful tool continues through the progress of theoretical and experimental efforts in several countries. The potential for military application of the FEL are more promising than other sources of directed energy. A major challenge to all high energy light sources is the complex effects of atmospheric propagation. Innovative beam relay methods may enable these obstacles to be minimized.

The proposed design of the CEBAF IR FEL will make important contributions toward realizing the goal of a high power, high efficiency source of coherent radiation for applications in medicine, industry, and possibly the military. Simulations of the CEBAF IR FEL in Chapters IV and V have contributed to the FEL design selection process. The broad tuning range of the CEBAF IR FEL was analyzed for system gain and power, and the influence of short electron pulse effects. The small electron beam of this system created strong distortion effects which were simulated in Chapter V. The interaction of the optical mode and the intense beam current resulted in higher FEL gain than predicted by single-mode gain theory. There exists a complex destructive interference in the optical mode that results in a radial "dimple" in the propagated wavefront. This phenomenon, and system gain, was explored in detail for single pass simulations in Chapter V and multiple passes in Chapter VI.



## LIST OF REFERENCES

- [1] J.M.J. Madey, "Stimulated Emission of Radiation in Periodically Deflected Electron Beams," *Journal of Applied Physics*, v.42, 1906, 1971.
- [2] N. Bloembergen, and others, "Report to the American Physical Society of the study group on science and technology of directed energy weapons," *Reviews of Modern Physics*, v.59, No.3 Part II, July 1987.
- [3] F. Gebhardt, "High Power Laser Propagation," *Applied Optics*, v.15 No.6, June 1976.
- [4] TRW Inc. Electronics and Defense Sector, *Ship Missile Defense Free Electron Laser*, S. Fornaca and H. Thompson, Jr., December 1, 1989,
- [5] J.W. Hardy, "Instrumental limitations in adaptive optics for astronomy," *Active Telescope Systems*, SPIE, v.1114, 1989.
- [6] J. Bell, *Thunderball*, W.J.Schafer Associates, 1901 North Fort Myer Drive, Arlington, Va 22209.
- [7] W.B. Colson, "Tutorial on Classical Free Electron Laser Theory," *Nuclear Instruments and Methods in Physics Research*, A237, 1985.
- [8] W.B. Colson and A.M. Sessler, "Free Electron Lasers," *Annual Review of Nuclear Particle Science*, v.35, 1985.
- [9] W.B. Colson, "Classical Free Electron Laser Theory", Chapter 5 in *Free Electron Laser Handbook*, W.B. Colson, C. Pellegrini and A. Renieri (eds.), North-Holland Physics, Elsevier Science Publishing Co. Inc., The Netherlands 1990.

- [10] Continuous Electron Beam Accelerator Facility, *High-Power UV and IR Free Electron Lasers Using the CEBAF Superconducting Accelerator*, Vol.1, Newport News, Va August 1991.
- [11] D. Clark and W.B. Colson, "The Cebaf Infrared Free Electron Laser," *Nuclear Instruments and Methods in Physics Research*, AXXX, xxxx-xxxx, 1992. accepted for publication December, 1991.
- [12] W. B. Colson and P. Elleaume, "Electron Dynamics in Free Electron Laser Resonator Modes," *Applied Physics B*, v.29, 101-109, 1982.
- [13] W.B. Colson and J.L. Richardson, "Multimode Theory of Free Electron Laser Oscillators", *Physics Review Letters*, v.50, 1050, 1983.
- [14] C.A. Bice and W.B. Colson, "The CEBAF Ultraviolet FEL Experiment," *Nuclear Instruments and Methods in Physics Research*, AXXX, xxxx-xxxx, 1992. accepted for publication December, 1991.
- [15] -M Tang and P. Sprangel, "The Three-Dimensional Non-Linear Theory of the Free Electron Laser Amplifier", *Physics of Quantum Electronics*, V. 9, *Free-Electron Generators of Coherent Radiation*, Addison-Wesley Publishing Company, Inc., 1982.
- [16] M. Xie, D.A.G. Deacon, J.M.J. Madey, *Nuclear Instruments and Methods in Physics Research*, A296, 672 (1990).

## INITIAL DISTRIBUTION LIST

- |    |   |   |
|----|---|---|
| 1. | Defense Technical Information Center<br>Cameron Station<br>Alexandria, Virginia 22304-6145                                    | 2 |
| 2. | Library, Code 52<br>Naval Postgraduate School<br>Monterey, CA 93943-5000  | 2 |
| 3. | Professor William B. Colson, Code PH/Cw<br>Department of Physics<br>Naval Postgraduate School<br>Monterey, CA 93943-5000      | 9 |
| 4. | Professor John R. Neighbours, Code PH/Nb<br>Department of Physics<br>Naval Postgraduate School<br>Monterey, CA 93943-5000     | 1 |
| 5. | Professor K.E. Woehler, Code PH/Wh<br>Chairman, Department of Physics<br>Naval Postgraduate School<br>Monterey, CA 93943-5000 | 1 |







Thesis  
C48074  
c.1

Clark

Theory for the CEBAF  
infrared and shipboard  
FELs. AF  
d

Thesis

C48074 Clark

c.1 Theory for the CEBAF  
infrared and shipboard  
FELs.



DUDLEY KNOX LIBRARY



3 2768 00033069 0